



LARGE SYNOPTIC SURVEY TELESCOPE

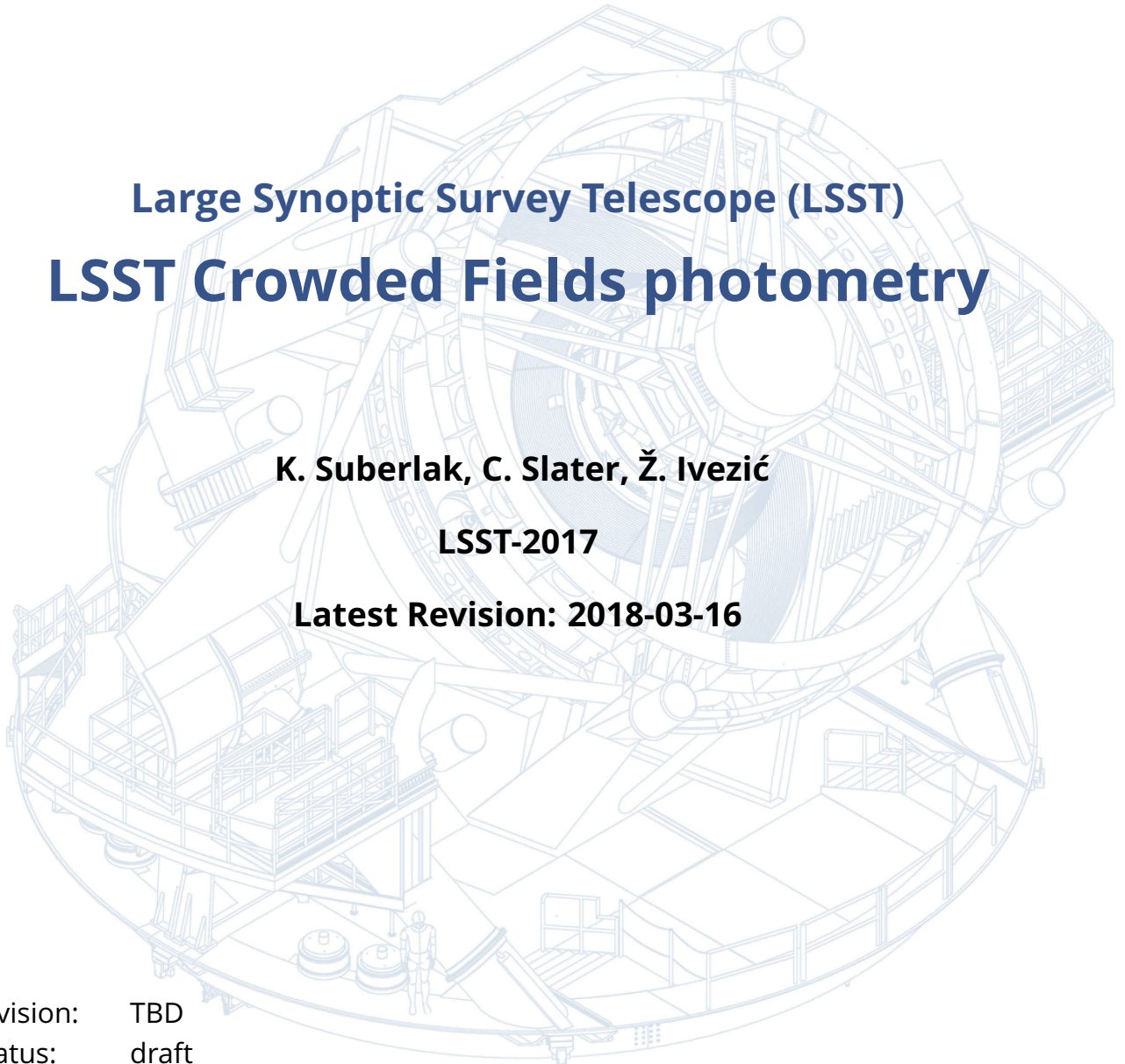
Large Synoptic Survey Telescope (LSST) LSST Crowded Fields photometry

K. Suberlak, C. Slater, Ž. Ivezić

LSST-2017

Latest Revision: 2018-03-16

revision: TBD
status: draft



Abstract

A report on the performance of current LSST Stack pipelines in crowded stellar fields. We use the DECAPS data to define the photometry and astrometry quality assurance metrics.

In the top 10% region, where DECAPS detects 200 000 sources per sq.deg., the mean LSST-DECAPS completeness in 18-20 mag is 80%, and it drops to 50% at 21.5 mag. For the same visit, the DECAPS 5σ limiting depth is 23 mag.

For a top 2% region, within the exclusion zone, in which DECAPS detects 500 000 sources per sq.deg., the mean completeness in 18-20 mag of LSST to DECAPS source-by-source is 78%, and it drops to 50% at 20.2 mag. For the same visit, the DECAPS 5σ limiting depth is 23.2 mag.

The systematic offset in photometry (the difference between the median photometric uncertainty and the measure of internal photometric repeatability) at 21 mag for the density of 200 000 sources per sq.deg. is 0.06 mag.

The LSST photometry is consistent with DECAPS. Above 19th mag, LSST and DECAPS are in systematics-dominated regime, consistent at 0.02 mag level. At fainter magnitudes, the scatter between LSST and DECAPS is less than the photometric uncertainty.

The spread of astrometric repeatability for LSST epoch-to-epoch is at the level of 10-30 milliarcsec, and is not strongly dependent on stellar crowdedness.

Change Record

Version	Date	Description	Owner name
1	2017-07-16	First draft.	Krzysztof Suberlak
2	2017-10-19	Updated outline.	Krzysztof Suberlak
2	2018-01-25	Major revision.	Krzysztof Suberlak
2	2018-03-04	Reorganized the draft.	Krzysztof Suberlak

Contents

1	Introduction	1
2	Identifying density regions	2
3	DECam Plane Survey	3
4	LSST Processing of DECAPS data	8
4.1	Cleaning DECAPS catalog, comparison to LSST pixel mask	8
4.2	Cleaning the LSST catalog	9
5	Source detection and photometry	19
5.1	Completeness	19
5.2	Photometry	19
6	Astrometry	25
7	Conclusions	36
7.1	LSST Processing of StarFast Simulated Sky	36
7.2	Other LSST-DECAPS tests: w-color	36

1 Introduction

We report on the performance of the Large Scale Synoptic Telescope (LSST) science pipelines¹, also known as ‘the LSST stack’, in the stellar fields of varying levels of source crowdedness.

The LSST will sample every night on average over 500 regions in the sky, delivering terabytes of raw data in need of processing, including photometric and astrometric calibration, to deliver a calibrated exposure image, as well as a source catalog, among image products² [7].

The survey sky is composed of regions very diverse in terms of stellar density, or crowdedness. Assuming the single-visit depth of 24.5 mag, the stellar density ranges from high density low-galactic latitude regions that have tens of millions of sources per square degree, to low-density regions towards the Galactic poles with less than thousand sources per square degree.

Deblending and successful photometry is an inherent part of any astronomical data processing pipeline. There exists a body of research answering questions that are specific to crowded stellar fields, eg. how many beams do we need per source [2], or how the crowded fields photometry can be approached in the era of large telescopes [8]. Other studies involving eg. HyperSuprime CAM pipeline (developed in parallel with the LSST Stack) recognized that the deeper the survey, the higher the stellar densities encountered, and therefore, the more challenging the process of deblending photometry [1].

In this report we compare the ‘out-of-the-box’ LSST Stack processing pipeline, to the DECam [Galactic] Plane Survey (DECAPS) catalogs based on the DECAPS pipeline developed by Schlafly et al. [9].

To find out where to look for regions representing various stellar densities, we use the Galfast simulation of the night sky (Sec. 2).

The Galfast simulation divided the sky into healpixels, which were used to select stellar fields representative of diverse stellar densities from the DECAPS image database (Sec. 3).

Finally, we compare the results of the LSST and DECAPS processing in terms of source detec-

¹<https://pipelines.lsst.io>

²<http://ls.st/LSE-163>

tion, photometry (Sec. 4), and astrometry (Sec.6). We conclude with key results and future work in Sec. 7.

2 Identifying density regions

To identify regions representing different stellar densities we use the LSST Galfast Metrics Analysis Framework³ simulated stellar density map prepared by P. Yoachim and L. Jones⁴

The resulting dataset `starDensity_r_nside_64.npz` contains 64 magnitude bins between 15 and 28 mag, with each bin containing the cumulative count of sources per square degree, with the entire sky divided into 49152 healpixels⁵ - see Fig. 1.

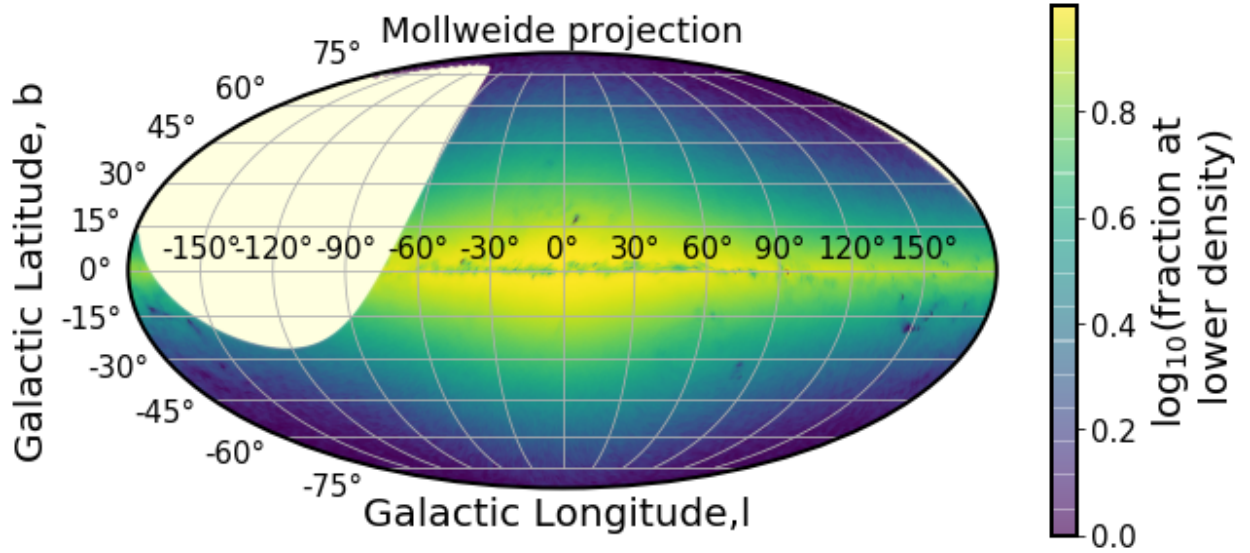


FIGURE 1: Galfast healpixels plotted in galactic coordinates in Mollweide projection. The brightest regions correspond to highest stellar densities. The missing part in the higher declination is the part of the sky above $\delta > 40^\circ$, which is not observable from the southern location of Cerro Pachón.

To match the LSST single-visit depth, we select magnitude bins smaller than $r=24.5$. For each healpixel we calculate the number of pixels that have a higher stellar count. Since each healpixel has an equal area, the fraction of pixel number above a certain threshold corresponds to the fraction of sky area above given density limit. Fig. 2 illustrates how we define

³<https://www.lsst.org/scientists/simulations/maf>, and https://github.com/lsst/sims_maf

⁴`sims_maf/python/lsst/sims/maf/maps/createStarDensitymap.py`

⁵<http://healpix.sourceforge.net>

percentiles of stellar densities, so that eg. 'top 1%' density means that only 1 in 100 pixels has a higher density than a given pixel, and 'top 10%' means that '10 %' of pixels in the considered simulation of the sky.

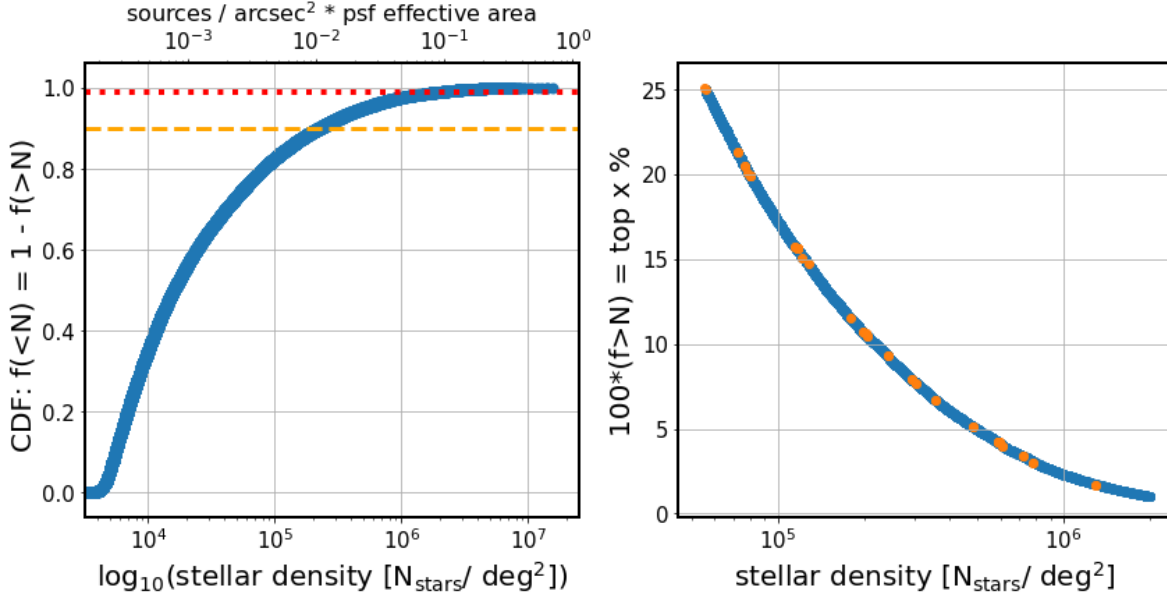


FIGURE 2: Using the Galfast sky simulation to choose DECAPS fields sampling different density regions. The left panel shows the stellar density as a function of the fraction of the sky at smaller density. It is equivalent to the cumulative distribution function. Given the stellar density per simulated healpixel, we count the number of healpixels at greater density. Normalized to the number of pixels, given their equal area, it corresponds to the fraction of the sky at greater stellar density. Horizontal dashed lines illustrate selecting pixels at top 1% or 10% density. The right panel focuses on the 1-CDF, converted to %, between 1 and 25%. It implies that according to the simulation, the density of 200 000 stars per sq.deg. corresponds to 5% of the sky, and only 1% of the sky has more than 10^6 stars per sq.deg. The upper axis represents the dimensionless demnsity parameter $N_{beam} = N_{stars}/arcsec^2 * A_{PSF}$, with the PSF effective area $A_{PSF} = 0.64arcsec$.

We illustrate the location of pixels representative of various density brackets on the sky in Fig. 3.

3 DECam Plane Survey

To analyze the performance of the LSST Stack with real data, we used the Dark Energy Camera (DECam) imaging, taken as part of the DECam Plane Survey (DECAPS) [9], at the 4-m Cerro Tololo Inter-American Observatory telescope (CTIO)⁶. On Fig. 4 we overlay the locations of all

⁶see <http://www.ctio.noao.edu/noao/node/1033>

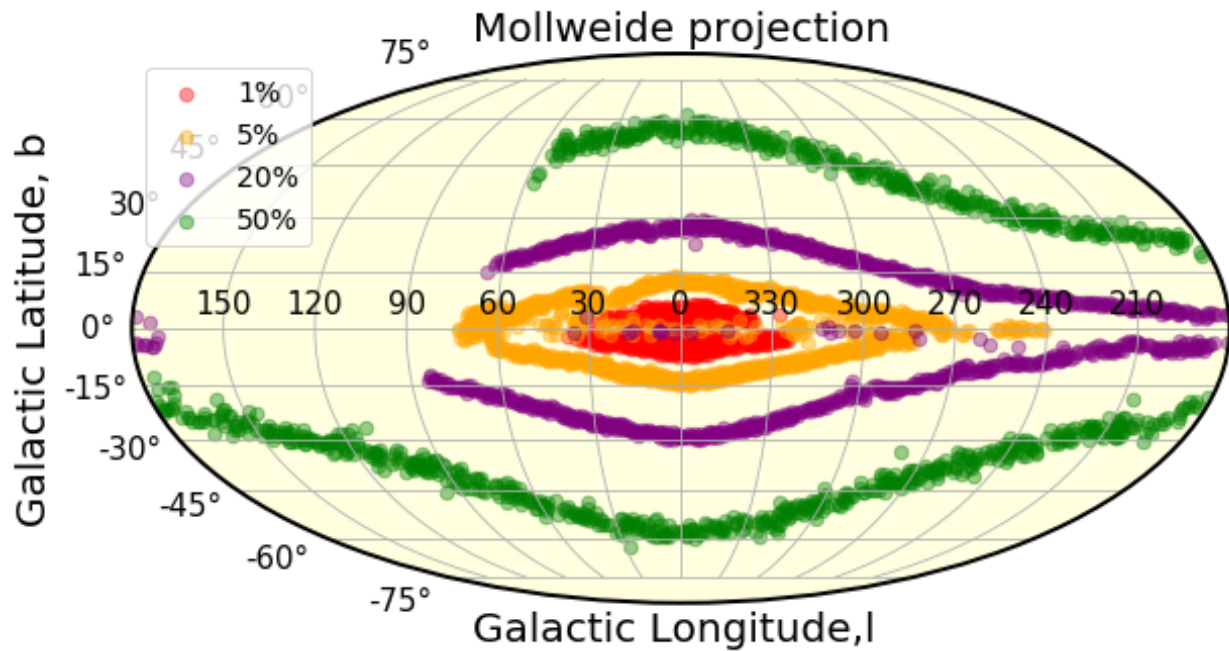


FIGURE 3: Illustration of location of regions representative of different relative simulated stellar densities in cylindrical projection, galactic coordinates. The x% region here means $x \pm 1\%$, eg. 5% includes regions between 4-6%. The highest density regions are located close to the galactic bulge, and regions of approximately constant stellar density trace isophotes of the Milky Way. The 20% regions close to the galactic equator correspond to high extinction regions that appear to have less counts due to interstellar dust. The galactic exclusion zone in LSST is closely follows the 5% region outline.

DECAPS fields on top the MAF map of the LSST sky. All DECAPS single-epoch images were processed with the DECAPS pipeline, resulting in single-epoch catalogs. The details of DECAPS pipeline can be found in Schlafly et al. 2017 [9]. DECAPS pipeline was specifically designed for crowded field photometry. It performs DAOPhot-like procedure ??, but does not use DAOPhot. The algorithm performs repeated source detection, subtraction, and re-detection, which is different from the LSST pipeline. DECAPS pipeline simultaneously solves for the positions and fluxes for all stars for a small fragment of the CCD (see Sec.4 in [9]). The headers of all DECAPS catalogs were assembled into the image database that contains information about single-visit exposure time, filter, time of observation, position, etc. We used the image database to select DECAPS fields with single-epoch depth similar to that of the single-visit depth of 30 sec LSST r-band exposure. Thus we selected DECAPS fields with exposure between 90 and 125 sec, taken in u, g, r, or VR filter.

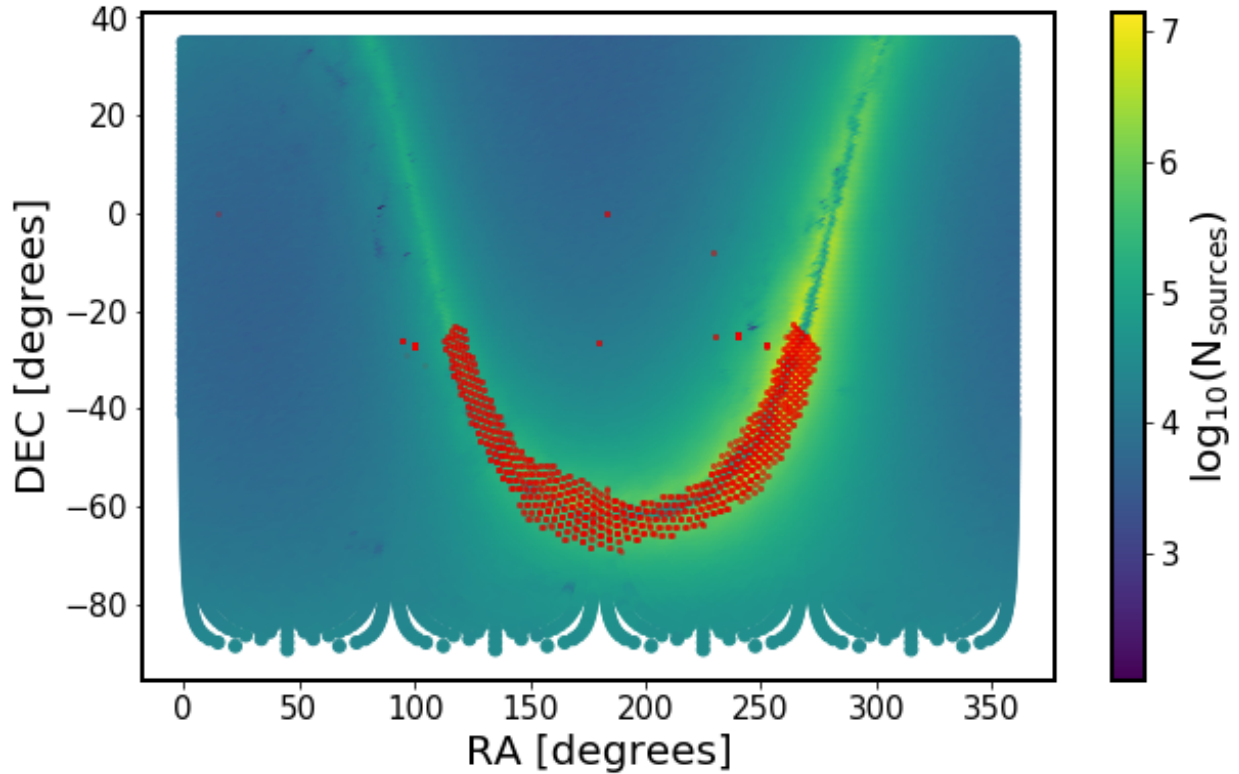


FIGURE 4: All DECAPS fields, overlaid on the map of healpixel stellar densities from MAF simulated sky. We matched the position of the center of each DECAPS field to the nearest healpixel to obtain an estimate of stellar density at each DECAPS field. In this way we selected DECAPS fields representative of various stellar densities (eg. 5%, 10%, 15%, as explained in Sec. 2).

We cross-matched the DECAPS image database with the stellar density information contained

in MAF healpixels. Each DECAPS image plane is tiled by a mosaic of 62 CCDs⁷. The size of each CCD element of the DECam image plane mosaic is 2046x4094 pixels, with pixel scale of 0.27 arcsec / px , so that a single mosaic element covers an area of 0.047117 square °. A single DECam exposure is also called a visit, and with 62 mosaic elements the full field of view 2.2°wide is several times bigger than the full moon. This makes it comparable to the LSST 3.5°wide field of view. Using the coordinates of the center of each DECAPS field we found the nearest healpixel within 0.5°.

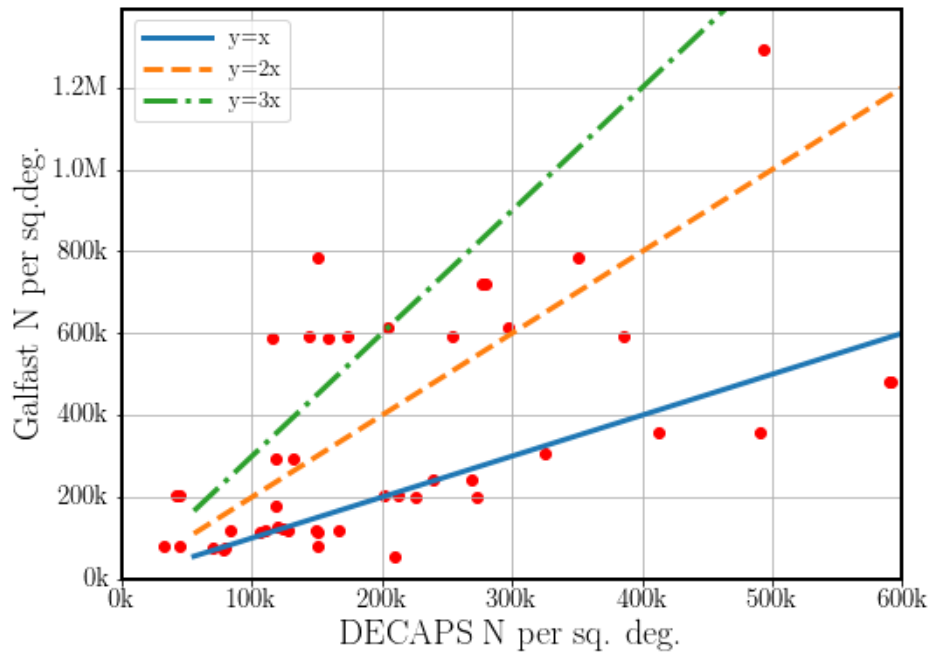


FIGURE 5: Comparison of DECAPS counts to Galfast simulated stellar counts. Overplotted are the line of equivalence $y=x$, and its multiplicities ($2x, 3x$). It shows that the simulation may be not more accurate than up to a factor of a few, but it is nevertheless useful for defining density regions. Part of the reason for discrepancy could be the order-of-magnitude nature of the experiment - Galfast counts here assume the single-visit depth of 24.5 mag in r-band. The DECAPS exposure time (≈ 100 sec) and filter (g, or r) were chosen to mimic that depth as closely as possible, but the regions targeted include much extinction, which means that in some cases DECAPS counts may be less than what is implied by the simulation. Different zero-point magnitude dependent on seeing conditions could also contribute to the depth probed by DECAPS. However, there is a number of fields that lie along the blue line, implying that in some cases the Galfast counts were very close to the true counts.

⁷See Fig.4-3 in the NOAO Data Handbook [10]

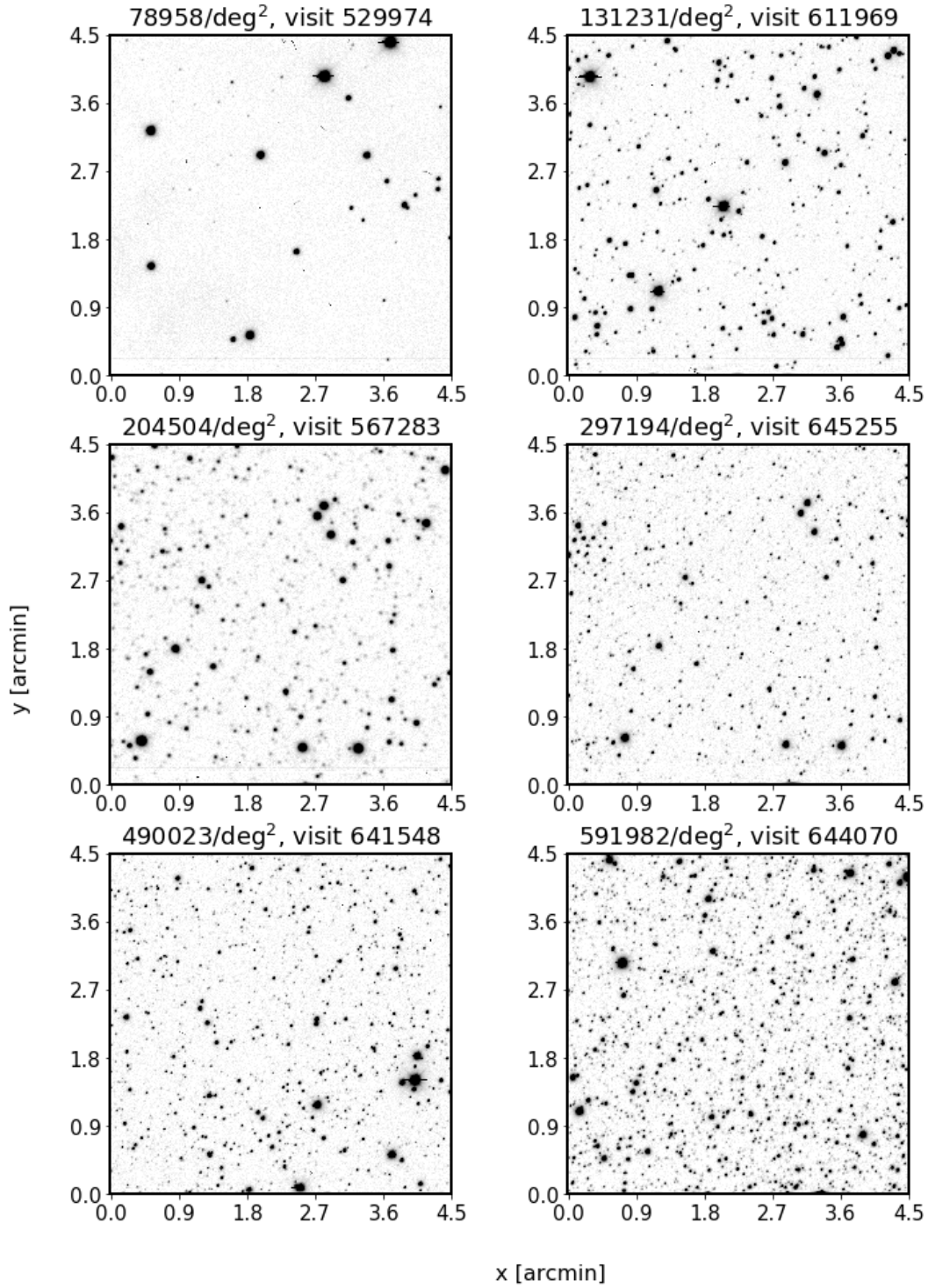


FIGURE 6: Illustration of regions of different stellar count in the cleaned DECAPS single-epoch catalogs. As shown on Fig. 5, the Galfast count (and therefore % level), does not always correspond 1:1 to the actual reported DECAPS stellar count. For this reason we simply ordered all DECAPS fields in terms of source count, and display postage stamp miniatures of CCD regions for visits in regions of increasing stellar density.

TABLE 2: LSST pixel mask bit values.

Bit position	Description	Mask decimal value
0	bad	1
1	saturated	2
2	interpolated	4
3	cosmic ray	8
4	edge	16
5	detected	32
6	detected negative	64
7	suspect	128
8	no data	256

4 LSST Processing of DECAPS data

The calibrated DECAPS imaging was processed with the LSST Science Pipelines installed on the LSST-dev machine at the NCSA⁸, with Stack version d_2017_10_27⁹. We specifically employed processCcd.py and the standard Stack configuration. Transferring the resulting source catalogs and calexp files to a local machine we analyzed the output of LSST processing using jupyter notebooks and custom python tools.

To compare single epoch DECAPS catalogs to LSST source catalogs we used the image mask, deblender flags, and other quality flags. The cleaning process is described in this section.

4.1 Cleaning DECAPS catalog, comparison to LSST pixel mask

To compare LSST and DECAPS catalogs, we cleaned both catalogs using the flag information assigned to each source by the respective image processing pipeline. To verify the validity of DECAPS source flags, we compared them with the LSST pixel-level mask information stored in the FITS Header Data Unit. Pixel-level masks are encoded in 8 bits, each of which can be 'on' or 'off', signifying that a given flag was 'on' or 'off' for a given pixel. The total value of the mask at each pixel is a decimal representation of such eight bits binary number, eg. $(00100001)_2 = 2^0 + 2^5 = 1 + 32 = (33)_{10}$ means that bit '0' and '5' are 'on' (counting from the right). See Table 2 for details.

⁸lsst-dev01.ncsa.illinois.edu (141.142.237.49) OS: CentOS 7.4.1708 HW: Dell Inc. CPU: 48x 2.60GHz RAM: 252 GB

⁹<https://eups.lsst.codes/stack/src/tags/>

TABLE 3: DECAPS flags. We excluded sources with flag bits 1,3,4,5,6,8,20,22.

Bit position	Description
1	Bad pixel
3	Saturated
4	Bleed trail
5	Cosmic ray
6	Low weight
8	Long streak
20	Additional bad pixel
21	Nebulosity
22	S7 amplifier B

For each visit we considered DECAPS single-epoch source catalog, and the LSST calexp image. We combined the calexp image mask value at the nearest pixel to every DECAPS source given its pixel coordinates. The bitwise 'and' of image mask with mask filter $(11011111)_2 = (2^1 + 2^2 + 2^3 + 2^4 + 2^6 + 2^7)_{10}$ (see Table 2 for details), flagged the source as 'bad' if either of the flag bits apart from '5' (detected) was 'on'.

Apart from LSST flags, each source also has a DECAPS pipeline flag, the value of which is made up of bits inherited from the NOAO Community Pipeline (see Table 3). We performed a bitwise 'and' of DECAPS flags with the mask filter $(2^1 + 2^3 + 2^4 + 2^5 + 2^6 + 2^8 + 2^{20} + 2^{22})_{10}$, flagging the source as 'bad' if either of these mask bits were 'on'.

Given the LSST and DECAPS flags, we compared which sources would be excluded based on the DECAPS source-level flags vs LSST pixel-level masks. We found for a random visit 611980 that the overlap between sources excluded by LSST pixel mask information versus DECAPS source flags is 99%. This means that the DECAPS flagging is consistent with the LSST image mask information, and the same sources would be 'excluded' based on either DECAPS flags or LSST mask information. For this reason we decided to clean the DECAPS catalog with source level flags, rather than the LSST image mask data.

4.2 Cleaning the LSST catalog

The LSST source catalog contains for each source a list of flags that could be set 'on' or 'off'. Of these, flags labeled `base_PixelFlags_flag` contain information relevant to the level of source detection, rather than processing (see Table 4).

TABLE 4: LSST source flags explanation.

name	explanation
flag	general failure flag, set if anything went wrong
offimage	Source center is off image
edge	Source is outside usable exposure region
interpolated	Interpolated pixel in the Source footprint
saturated	Saturated pixel in the Source footprint
cr	Cosmic ray in the Source footprint
bad	Bad pixel in the Source footprint
suspect	Source's footprint includes suspect pixels
interpolatedCenter	Interpolated pixel in the Source center
saturatedCenter	Saturated pixel in the Source center
crCenter	Cosmic ray in the Source center
suspectCenter	Source's center is close to suspect pixels
flag	General Failure Flag

We clean the LSST source catalog by removing sources that have flags 'edge' or 'interpolated-Center'¹⁰. Other flags would remove too many sources that have only small defects, eg. flag 'interpolated' may be on for a bright source across the footprint of which there is a cosmic ray, while flag 'bad' may be on for any source which has even one bad pixel in the footprint. A comparison of the initial source count to the final source count (after cleaning) is shown on Fig. 9, with detailed counts in Table 5.

¹⁰This is similar to the example in Sec.4 of SDSS Image Processing I: The Deblender [3]

Visit	N_{raw}	(N_f)	$-N_r$	$= N_c$	N_c/deg^2	N_{MAF}/deg^2	ρ_{MAF}	N_{loSN}	$N_{parents}$	$N_{blended}$	$N_{deblended}$
568172	29809	9148	12434	17375	6241	72072	21.3	12986	153919	77723	289200
527319	120862	13744	39638	81224	29175	79632	19.9	34282	112848	28212	86196
530012	160406	15210	61337	99069	35585	203040	10.6	51669	20425	2143	7241
525846	167582	15247	63295	104287	37459	203040	10.6	51949	96932	31724	113865
525900	171337	15037	58219	113118	40631	79632	19.9	46796	70011	9731	41120
529989	182933	15910	61808	121125	43508	79632	19.9	49120	114760	54746	198511
529974	228849	16842	67339	161510	58014	76572	20.5	44712	104406	26981	103920
525814	235307	16811	72214	163093	58582	76572	20.5	50998	98063	28128	102658
527096	227256	16100	59686	167570	60191	55908	25.0	36748	85483	16136	69718
644125	242521	16387	72363	170158	60101	72072	21.3	40731	89237	17861	75835
611980	273032	18816	76043	196989	70758	116856	15.6	41383	78662	42516	151854
527247	264383	15283	66539	197844	71065	116676	15.6	38391	138758	59728	200438
567283	280305	16981	68379	211926	76123	612648	4.0	30908	230049	64593	195501
527555	313294	1173	81585	231709	83229	783324	3.0	39458	127709	49579	170745
612757	317270	4014	84877	232393	82084	292788	7.9	42468	128543	50645	176673
527246	319929	18136	86268	233661	83930	114588	15.7	47233	128325	58651	206903
640891	355861	24520	107462	248399	87737	121536	15.1	60163	127665	45693	146571
611970	377917	26716	120640	257277	92413	178992	11.5	80884	133384	53522	184423
645251	348033	18786	89669	258364	91257	128016	14.7	41210	129397	34130	100856
527296	361951	21167	101452	260499	93571	588096	4.2	63149	144777	50631	182509
611969	387056	25752	118639	268417	96415	292788	7.9	74291	162439	70305	262885
526413	368017	22267	98745	269272	96722	78480	20.1	52626	151602	82678	295547
525838	371329	19984	100644	270685	97229	116676	15.6	54839	71782	16117	79683
525837	393879	22350	107414	286465	102898	114588	15.7	56743	74171	14580	71655
611529	398924	22625	105677	293247	105334	116856	15.6	54741	113152	86539	376291
527552	395446	1716	99214	296232	106406	591336	4.2	44093	95415	72727	318061

525920	415231	22439	111423	303808	109127	588096	4.2	59375	133660	55280	198116
527300	436689	24839	120330	316359	113635	594324	4.2	70470	170980	82687	317507
644035	435830	2170	106363	329467	116371	205308	10.5	46535	93985	48307	174978
525904	479294	26679	135534	343760	123478	594324	4.2	77080	112960	67743	255127
527453	495629	28732	139172	356457	128039	242316	9.3	80487	208259	137811	565651
609754	490143	26233	121738	368405	132330	116856	15.6	62319	199832	151565	653749
530032	486203	23112	115217	370986	133257	198432	10.7	51002	176645	113085	441312
526152	520842	28739	143336	377506	135599	55404	25.1	77724	142876	100061	400366
567795	508405	26663	129592	378813	136069	721728	3.4	63447	62120	42489	175696
641497	529827	28546	137626	392201	138530	205308	10.5	59868	184493	139641	592661
640995	571174	2973	155705	415469	146748	242316	9.3	85262	171899	67666	239729
527064	558264	26197	132299	425965	153006	591336	4.2	56098	184352	59068	193269
566793	560376	1088	134186	426190	158458	1292976	1.7	59842	132416	60622	222193
644205	571378	4663	142463	428915	151498	721728	3.4	65955	165636	45858	150457
525879	575982	28502	139102	436880	156927	198432	10.7	63181	119515	85247	353502
644144	597726	30439	152632	445094	168442	1292976	1.7	77506	115951	62116	217379
644082	614401	29828	152226	462175	163246	783324	3.0	65428	166750	94046	356549
645255	617345	2342	148062	469283	165756	612648	4.0	62971	187074	140722	589579
644011	643303	5962	151827	491476	173595	355896	6.7	58686	129561	76106	302738
641500	731042	2925	178763	552279	195071	305280	7.7	78451	171114	92824	350463
526028	911721	38810	234490	677231	243260	305280	7.7	113255	166673	85331	319374
644074	916795	41973	219530	697265	246282	481788	5.1	89471	102816	48459	162019
644070	917375	3993	214363	703012	248312	481788	5.1	87108	122274	89793	385659
641548	1005146	44347	238787	766359	270687	355896	6.7	96812	117637	85174	357565

Table 5: A summary of all LSST-processed DECAPS visits. The column ‘visit’ corresponds to the DECAPS visit number. The following four columns (‘N raw’, ‘N f’, ‘N r’, ‘N c’) contain the source counts per visit area ($\approx 2.74 \text{ deg}^2$). ‘N raw’ is the input number of sources per visit, summing over all CCD source catalogs. ‘N f’ is the number of sources removed due to bad flags. ‘N r’ is the total number of removed sources (due to flags, low S/N, or sources that in the LSST deblending process are neither isolated parents, nor deblended children). ‘N c’ is the final number of clean sources per visit (‘N raw’ - ‘N r’ = ‘N c’). ‘N c/deg²’ is ‘N c’ converted to count per deg². N_{MAF}/deg^2 is the predicted number of sources per deg² at that location based on Galfast simulation. ρ_{MAF} is the MAF density; eg. 21.3 is the top 21.3% stellar density of the simulated sky.

Visit	N_{raw}	(N_f)	$-N_r$	$= N_c$	N_c/deg^2	N_{MAF}/deg^2	ρ_{MAF}
568172	16824	138	150	16674	5989	72072	21.3
527319	92326	2819	3039	89287	32071	79632	19.9
530012	121313	3293	3982	117331	42145	203040	10.6
525846	125245	3135	3457	121788	43746	203040	10.6
525900	127722	2557	2786	124936	44876	79632	19.9
529989	140043	2527	2803	137240	49296	79632	19.9
527096	194837	2126	2290	192547	69162	55908	25.0
525814	200562	4481	4938	195624	70268	76572	20.5
529974	224231	3992	4413	219818	78958	76572	20.5
644125	228088	5570	6182	221906	78380	72072	21.3
527247	237656	4858	5144	232512	83518	116676	15.6
527246	301083	5469	5907	295176	106027	114588	15.7
611980	315722	6779	7397	308325	110750	116856	15.6
527296	330295	7176	7726	322569	115866	588096	4.2
611970	340528	9668	10513	330015	118541	178992	11.5
612757	342629	8541	9473	333156	117674	292788	7.9
645251	343358	5546	6253	337105	119069	128016	14.7
640891	361837	9423	10389	351448	124135	121536	15.1
525838	360793	6057	6515	354278	127256	116676	15.6
611969	376588	10280	11243	365345	131231	292788	7.9
527300	409385	8974	9654	399731	143583	594324	4.2
611529	428299	9981	11167	417132	149833	116856	15.6
527555	421706	3848	4285	417421	149937	783324	3.0
525837	425261	6791	7437	417824	150082	114588	15.7
526413	428035	8417	9137	418898	150467	78480	20.1
525920	449868	6675	7430	442438	158923	588096	4.2
609754	474355	10034	11677	462678	166193	116856	15.6
525904	490306	8413	9118	481188	172842	594324	4.2
567283	575760	5549	6426	569334	204504	612648	4.0
644035	583432	9457	10948	572484	202208	205308	10.5
526152	599164	12579	14023	585141	210182	55404	25.1
641497	611424	10156	11324	600100	211962	205308	10.5
530032	638179	9776	10964	627215	225295	198432	10.7
527453	682113	14654	16569	665544	239062	242316	9.3
527552	714305	6031	6893	707412	254101	591336	4.2

525879	772457	11625	13117	759340	272754	198432	10.7
640995	783011	17946	20850	762161	269204	242316	9.3
567795	791019	9439	11056	779963	280162	721728	3.4
644205	800175	13601	15899	784276	277016	721728	3.4
645255	852539	9620	11135	841404	297194	612648	4.0
641500	935661	14131	16133	919528	324788	305280	7.7
644082	1007998	12826	15633	992365	350515	783324	3.0
526028	1035808	17929	20772	1015036	364600	305280	7.7
527064	1085375	10200	12399	1072976	385412	591336	4.2
644011	1181972	11059	13806	1168166	412611	355896	6.7
566793	1350724	12414	22431	1328293	493863	1292976	1.7
641548	1404895	14336	17562	1387333	490023	355896	6.7
644144	1444897	16255	28641	1416256	535971	1292976	1.7
644074	1692430	16941	23670	1668760	589427	481788	5.1
644070	1698554	16404	22559	1675995	591982	481788	5.1

Table 6: A summary of all single-epoch DECAPS source catalogs, with columns as in Table 5. See Fig. 9 comparing the 'N raw' converted to number of sources per square degree, and 'N clean per sq.deg.'.

Given the single-epoch DECAPS source catalogs, and the LSST source catalogs, we followed a uniform set of procedures to clean both datasets, and in turn cross-match positionally. First we made a quality cut removing all sources with signal-to-noise ratio smaller than five: $S/N < 5$. The number of sources thus removed depends on a visit number, but does not exceed few % of the catalog. Following that we also removed sources with flags that correspond to bad, edge detections, cosmic rays, or saturation spikes (as outlined in Sec. 4.1 and 4.2). The LSST Processing Pipeline deblends sources in a similar fashion to the SDSS Imaging Pipeline¹¹. For the LSST source catalog, we chose to keep only those sources that were either isolated parents (parentId=0, nchild=0), or deblended children (parentId != 0, nchild=0) (see Table 7 for details.)

¹¹SDSS Image Processing I: The Deblender [3], SDSS Image Processing II: The Photo Pipelines [4], [6], and [5]

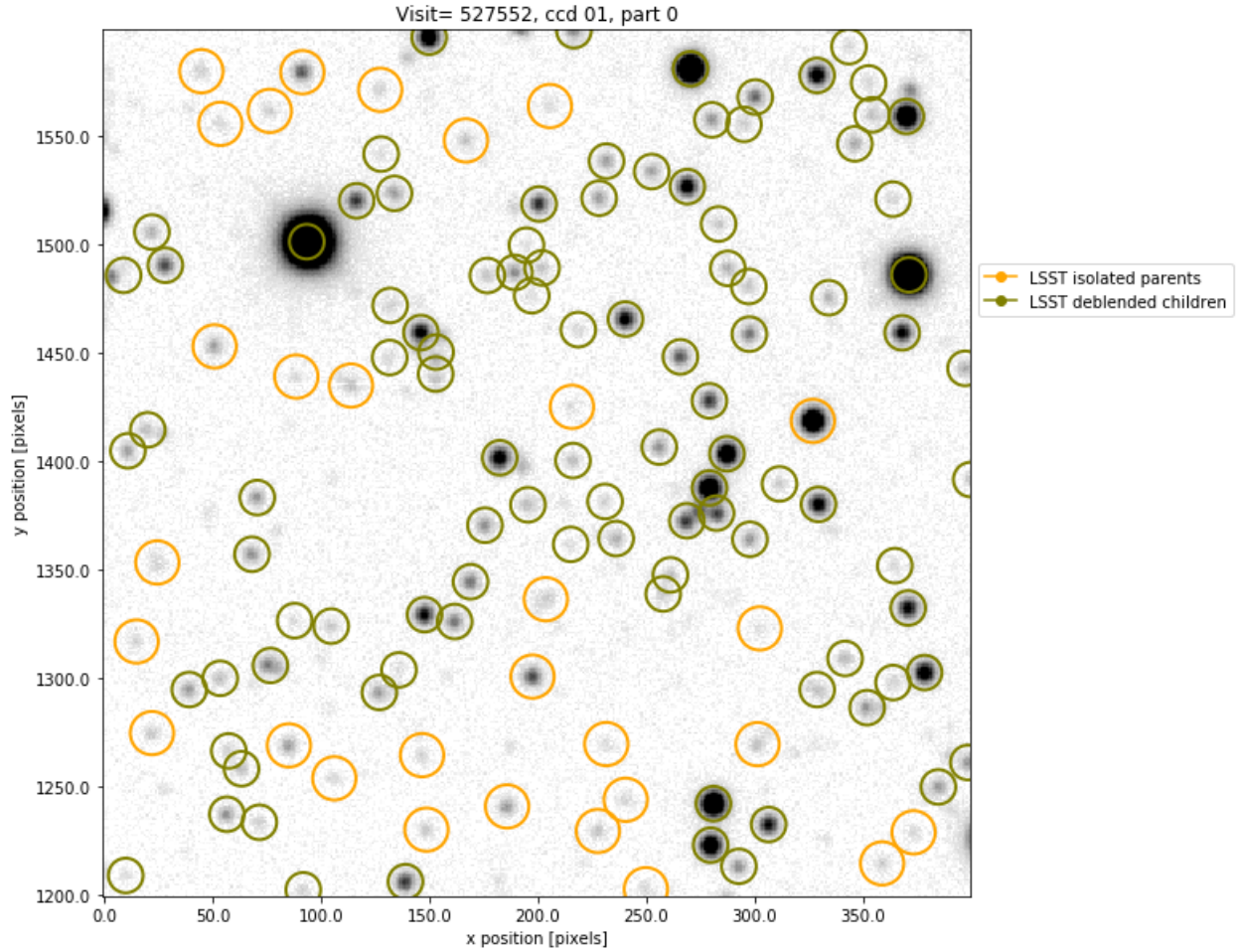


FIGURE 7: We illustrate the sources as reported by the LSST pipeline for a small region of CCD01 of visit 527552. A source may be reported as an isolated source (yellow), or a successfully deblended child (green). In this analysis we only keep isolated parents or deblended children.

TABLE 7: Summary of possible parentID and nchild combinations for blended sources in the LSST Science Pipeline. An example count in the final column is provided for visit 525814, a top 20% density region, which has the raw source count 235307. For that visit 16811 sources had bad flags, 49901 had $S/N < 5$, and in total 163093 were kept in the clean catalog.

parentID	nchild	type	decision	count
0	0	parent: isolated source	keep	104406
0	>0	blended source	remove	26981
!=0	0	deblended child	keep	103920
!=0	>0	failure case	remove	0

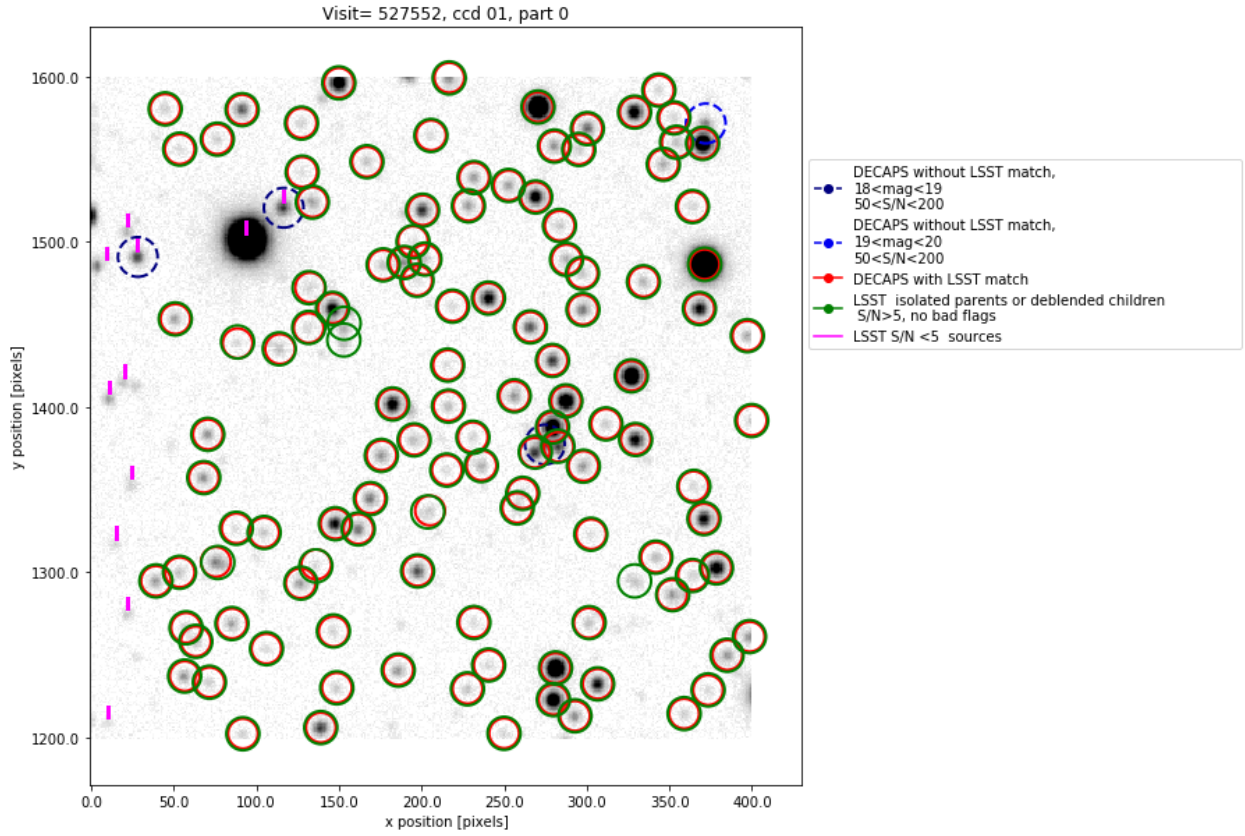


FIGURE 8: The same region as on Fig. 7. Green circles mark the position of retained LSST sources: isolated parents, or deblended children, with $S/N > 5$, and no bad flags. Red circles mark the position of DECAPS detections with an LSST match. Vertical magenta dashes are above the LSST sources with $S/N < 5$. Blue dashed circles mark location of DECAPS source without an LSST match. Note that eg. at $(x,y) = 50,1490$ an LSST source was detected, but since its $S/N < 5$ it was not kept in the clean LSST catalog.

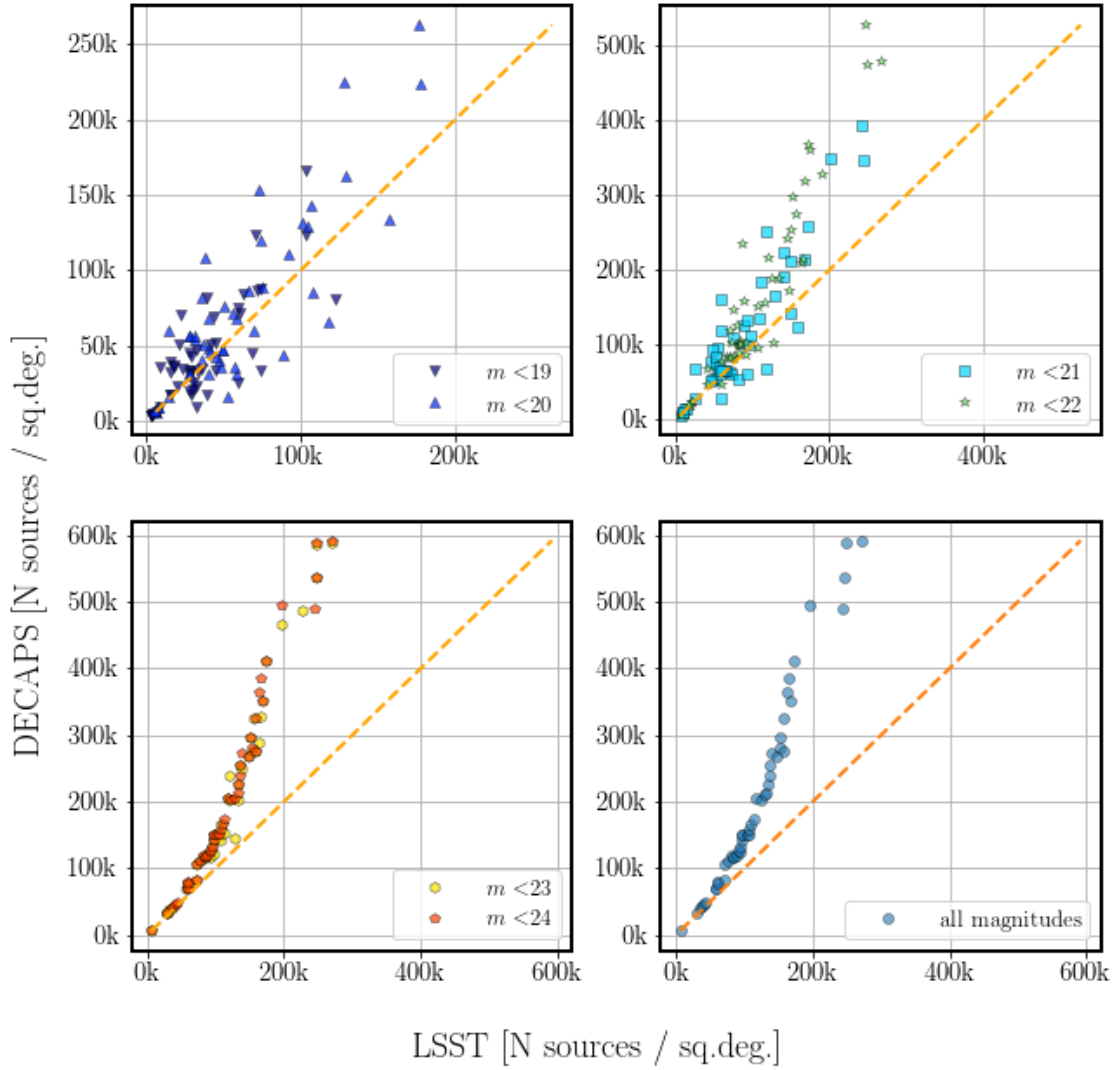


FIGURE 9: A plot of source count comparing LSST to DECAPS source catalogs of the same fields (visits). On each panel we plot the number of counts up to a given magnitude, increasing the depth clockwise. The bottom right panel shows all sources without magnitude limits. For exact counts in each stellar field, see Tables 5 and Table 6.

5 Source detection and photometry

Starting with cleaned LSST and DECAPS source catalogs, we consider a set of metrics to compare the quality of LSST science pipelines to the state-of-the-art DECAPS pipeline.

5.1 Completeness

For each visit that corresponds to a given level of crowdedness, we consider the detection completeness of LSST to DECAPS. Assuming that DECAPS is the ‘true’ catalog of sources, we define completeness by the percentage of DECAPS sources (binned along DECAPS magnitude), that have an LSST match within $0.5''$. This is a very liberal requirement considering that for most visits $>98\%$ of DECAPS sources have an LSST match within $0.3''$. Second, we require that the sources differ by not more than 0.5 magnitudes. As illustrated on Fig. 13, this only removes the outliers. In fact, given that the majority of the sources ($>99\%$) that are matched within $0.5''$, do not differ by more than 0.5 magnitude, this constraint does not change the completeness by more than few %. Fig. 10 shows how completeness, and catalog counts, depend on source density.

5.2 Photometry

We consider here photometric accuracy. Since both DECAPS and LSST processing pipelines start from the same instcal calibrated DECam images, they ought arrive at similar measurement of flux, and in turn, instrumental magnitudes.

An offset and a spread in magnitude difference is due to details of each image processing pipeline.

We compare the photometric repeatability within each pipeline, as well as the existence of offset and spread between two different pipelines. We test pipeline repeatability by investigating two visits at the same locations, taken in same filters, with equal exposure times. Assuming that the majority of objects are non-variable in nature, we find the statistical epoch-to-epoch variance.

Using the DECAPS image database for several visits we found a second visit at exactly the same location, filter and exposure time, but different epoch (see Table 8). This allowed to

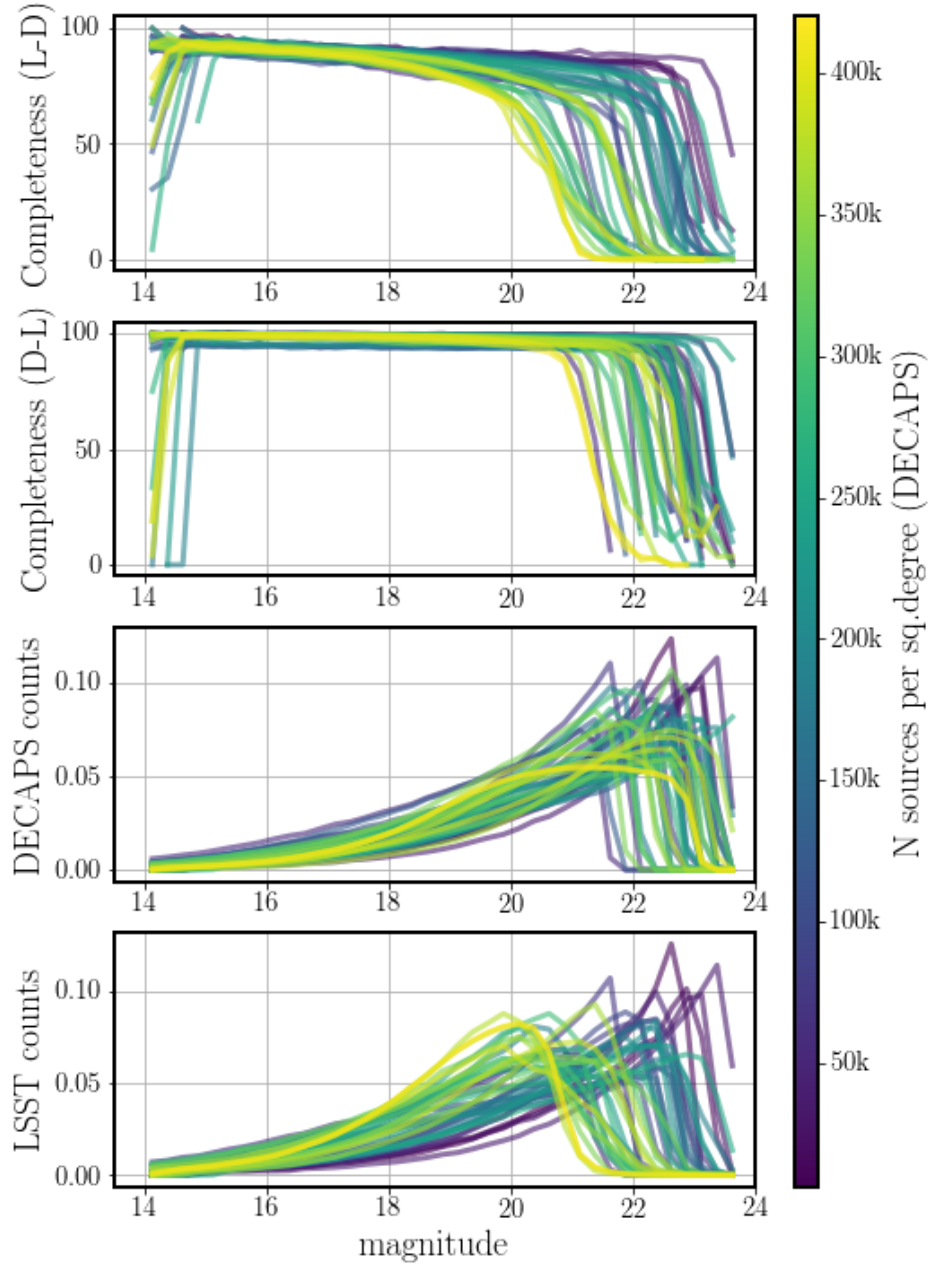


FIGURE 10: Top two panels show source-to-source completeness. The first panel is a measure of how complete is LSST catalog to DECAPS catalog (L-D), i.e. the fraction of DECAPS sources per magnitude bin that have an LSST match. The second panel shows an equivalent plot for the completeness of DECAPS to LSST (D-L), plotting the fraction of LSST sources that have a DECAPS match. The bottom two panels show the normalized source counts in the input catalogs. The LSST-DECAPS completeness falls off quicker than DECAPS-LSST, since DECAPS catalog has more sources at fainter magnitudes (see Fig. 9). Different colors correspond to different level of stellar crowdedness, expressed in terms of the number of sources per square degree in DECAPS clean catalogs. We further characterize completeness by $\langle C_{18-20} \rangle$ - the mean completeness between 18-20 mag, and m_{50} - the magnitude at which completeness falls to a 50% level (see Fig. 11)

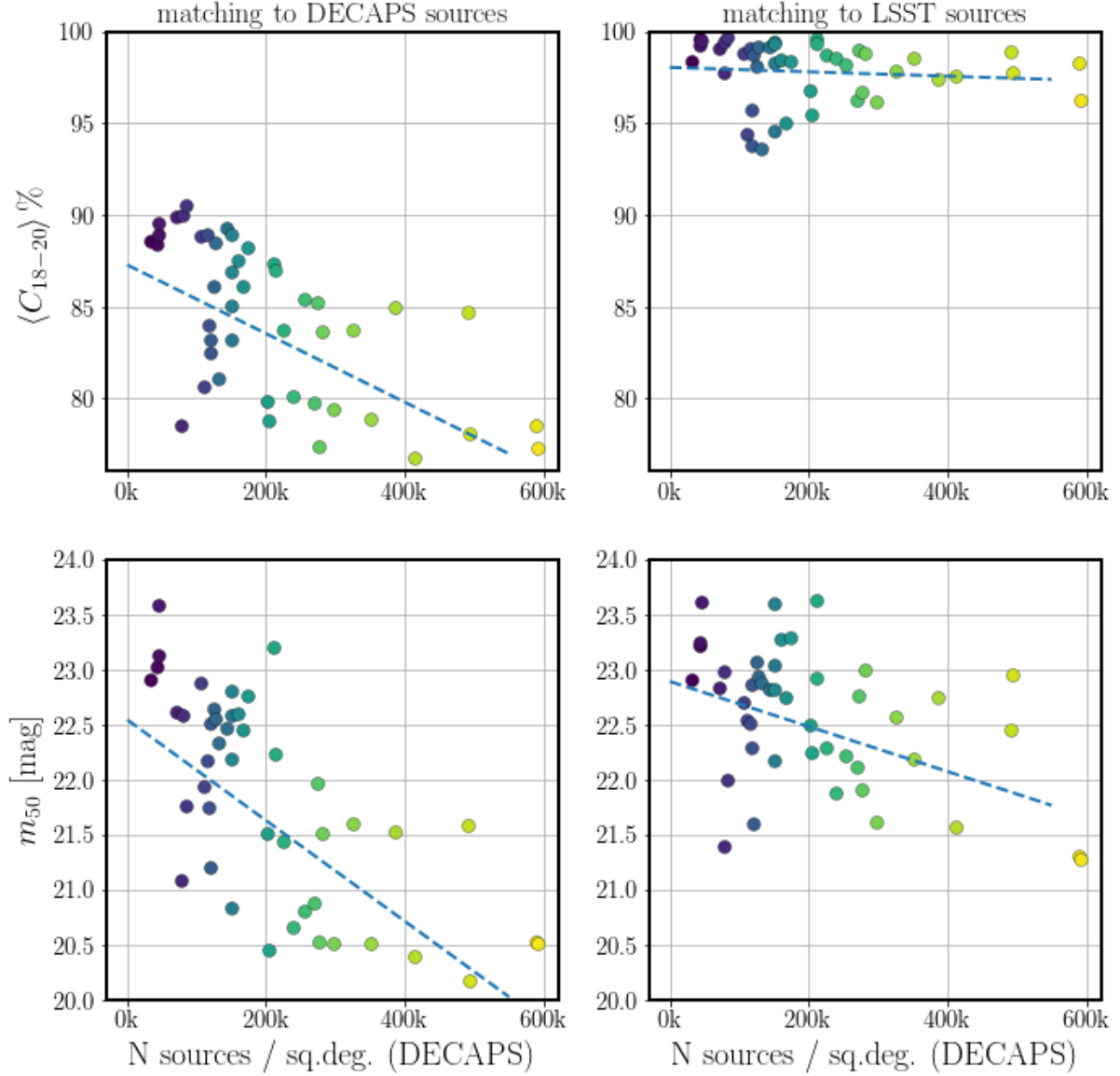


FIGURE 11: Magnitude at which completeness falls to 50% (top two panels), and the mean completeness between 18 and 20 magnitudes (bottom two panels). The panels on the left hand side correspond to the uppermost panel in Fig. 10, while the right hand side panels correspond to the second panel in Fig. 10. The color of all points corresponds to the stellar density, as in Fig. 10. In each panel we overplot the linear best-fit to indicate the expected overall trend of decreasing $\langle C_{18-20} \rangle$ and m_{50} with source density.

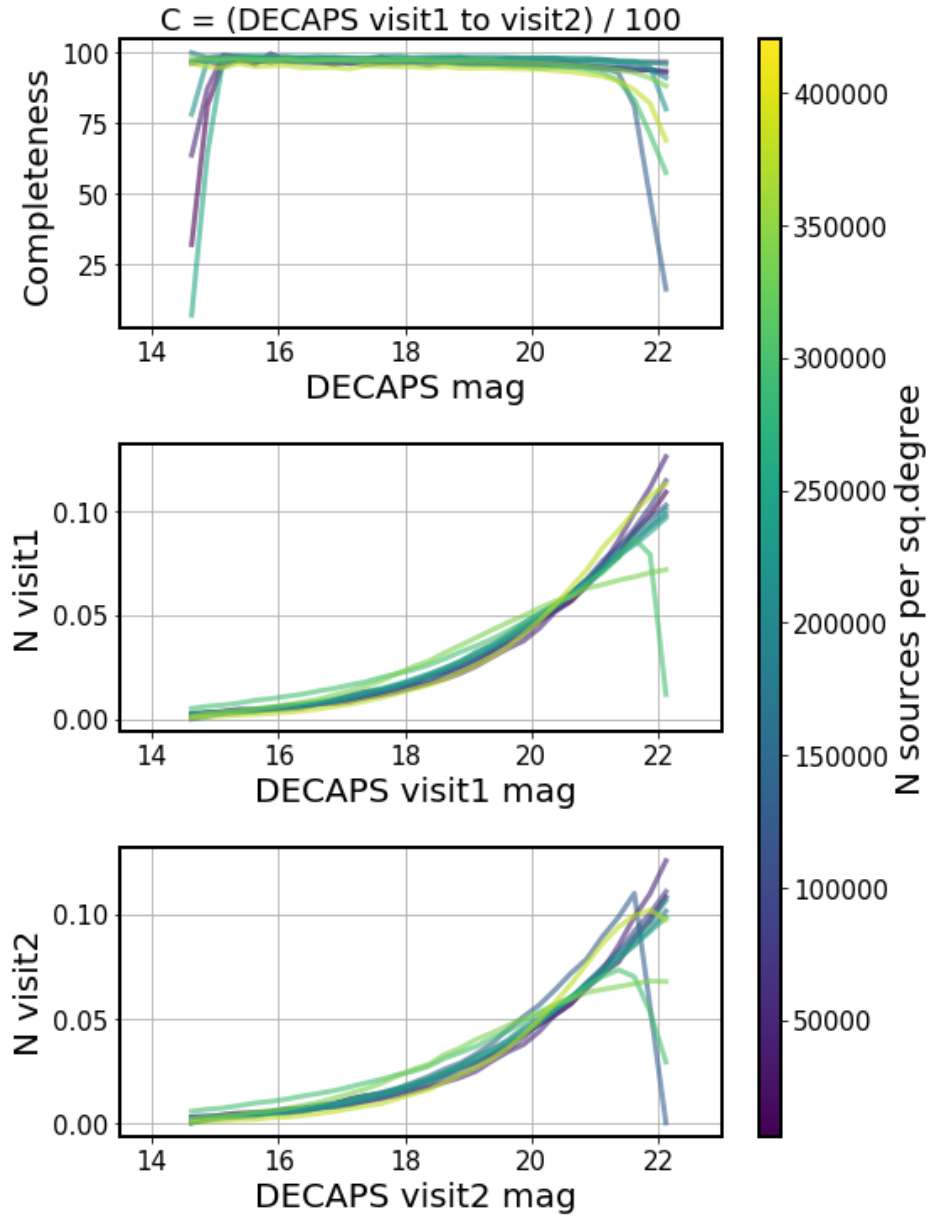


FIGURE 12: The same quantities as on Fig. 10, but corresponding to two different visits at the same location, to test the repeatability of DECAPS detections. The two visits (visit1, visit2) were chosen in the same filter and at the same location, and as in tests for completeness, we match source-by-source and consider the number of sources per magnitude bin in visit1 that do have a matching source in visit2.

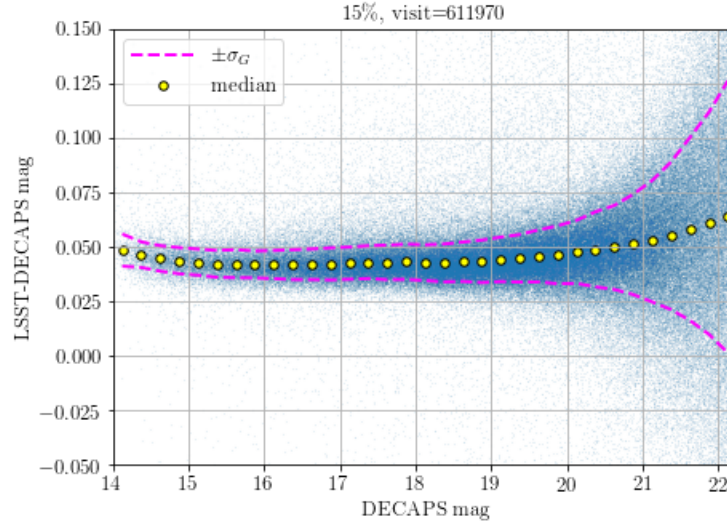


FIGURE 13: Difference in magnitudes between the DECAPS and LSST magnitudes for sources matched within 0.5 " for a region in top 15% density (611970). The magenta dashed line traces the $\pm\sigma_G(\Delta m)$ level, and yellow circles the median. $\sigma_G = 0.7413 * (q75 - q25)$, where $q75$ and $q25$ are 75th and 25th percentiles, is an interquartile-based measure of standard deviation, that is insensitive to the outliers. For this stellar density, the offset between LSST and DECAPS is on the level of 0.05 mag. The same quantities (σ_G , median(Δm)) plotted for fields of various stellar densities are shown on Fig. 15. The histograms of Δmag per magnitude bin are shown on Fig. 14.

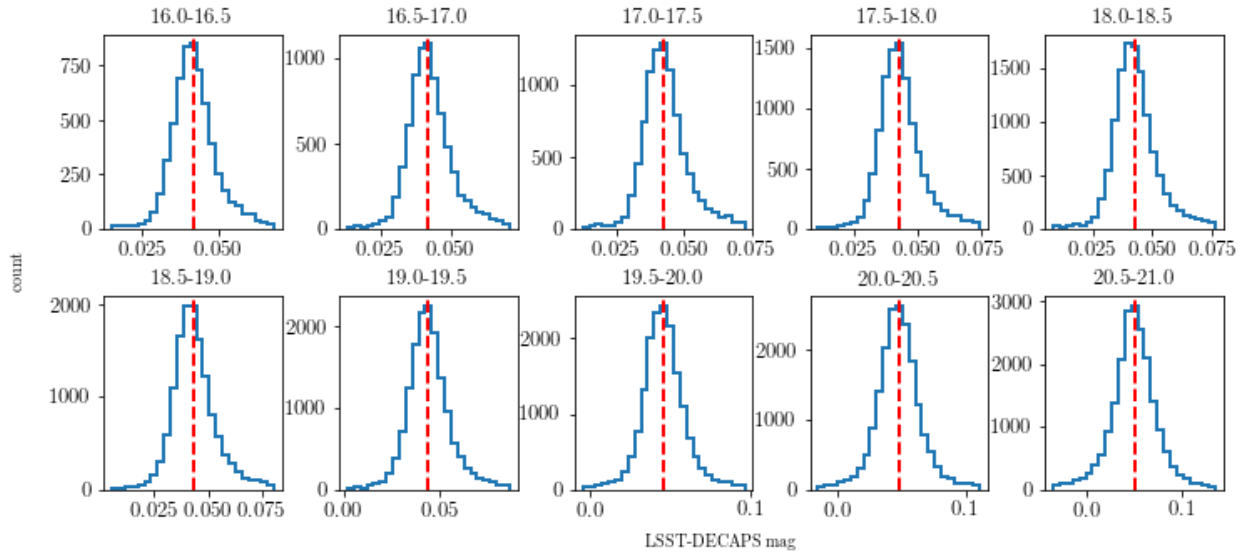


FIGURE 14: Cross-section of Fig. 13, showing the histogram of Δmag per DECAPS magnitude bin. The vertical red line corresponds to the median value of Δmag in that bin, and each histogram is limited between $\pm 4\sigma_G$.

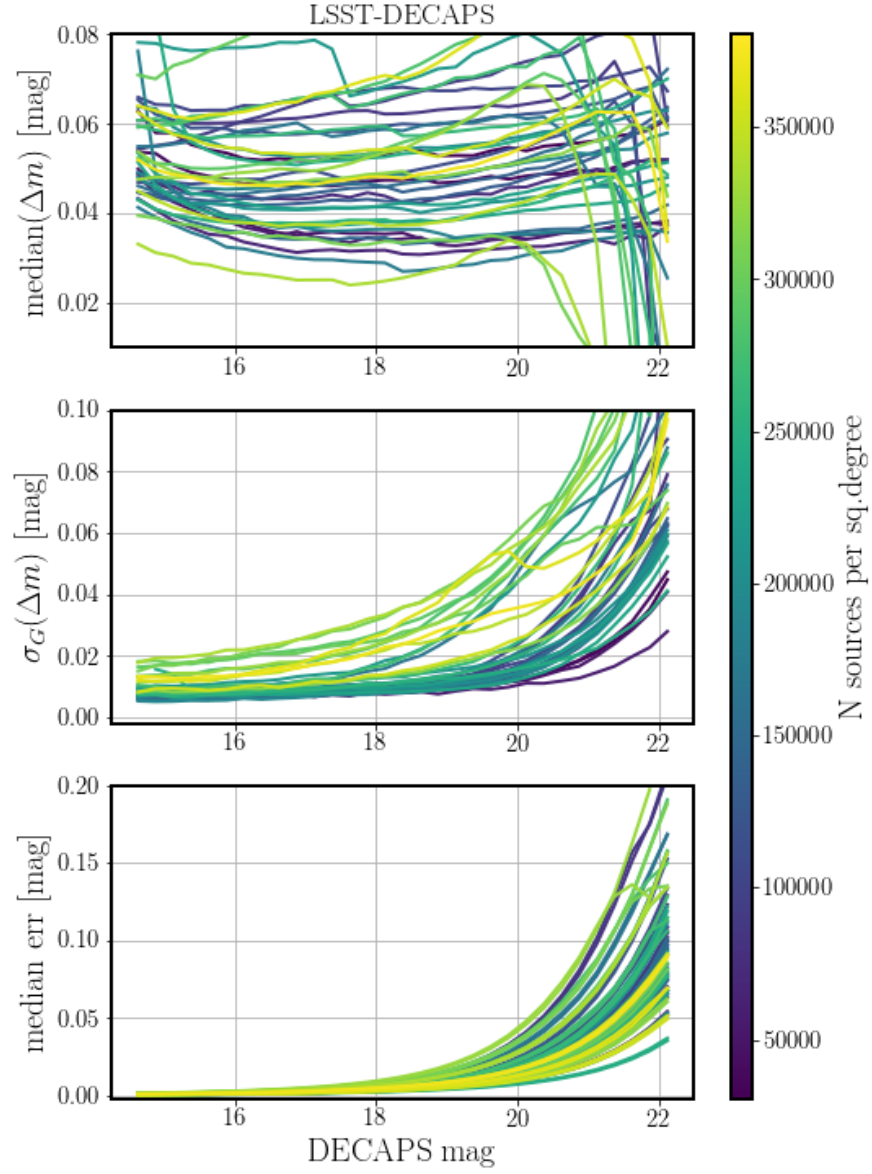


FIGURE 15: The measurement of photometric offset between DECAPS and LSST pipelines. For each visit we cross-matched source catalogs corresponding to LSST and DECAPS processing; Δm is the difference in magnitude reported between DECAPS and LSST for the same source. For each visit we bin sources according to their DECAPS magnitude. On three panels we plot the binned statistics : $\text{median}(\Delta m)$, $\sigma_G(\Delta m)$, and median photometric uncertainty.

TABLE 8: Pairs of visits at two different epochs, arranged by the mean LSST-DECAPS source density (last column). The RA and DEC are in degrees, and mean source density $\langle N_{1,2} \rangle$ in sources per sq. deg.

visit1	ra1	dec1	visit2	ra2	dec2	$\langle N_{1,2} \rangle$
525846	133.55	-44.27	530012	133.55	-44.27	39733
525900	140.62	-48.15	529989	140.62	-48.15	44577
525814	126.43	-43.07	529974	126.42	-43.07	66455
525838	132.59	-50.3	527247	132.59	-50.31	94766
611969	115.53	-24.08	612757	115.79	-24.11	106851
525837	131.56	-48.6	527246	131.56	-48.6	110734
525920	143.23	-51.45	527296	143.23	-51.45	119371
525904	140.55	-51.25	527300	140.55	-51.25	138384
641497	166.47	-53.71	644035	166.73	-53.8	167267
567283	247.04	-47.27	645255	247.03	-47.27	185894
644082	190.31	-61.09	527555	190.32	-61.09	186731
527453	173.92	-62.16	640995	173.91	-62.16	195763
525879	137.64	-54.08	530032	137.64	-54.09	197058
567795	252.15	-47.43	644205	251.81	-47.41	211186
527064	189.89	-59.43	527552	189.88	-59.43	224731
526028	168.47	-56.53	641500	168.47	-56.52	281929
641548	176.18	-66.43	644011	176.46	-66.52	336729
644144	243.08	-53.37	566793	243.08	-53.37	339183
644074	188.49	-67.28	644070	188.18	-67.23	419000

test the epoch-epoch photometric repeatability of DECAPS-LSST. We illustrate the magnitude differences on Figs. 16 and 17, and the summary of the spread of photometric difference as a function of magnitude on Figs. 18 and 19.

We summarize the information about the photometric repeatability (epoch-to-epoch within a given pipeline), and offset (pipeline-to-pipeline of the same epoch), by combining information from Figs. 15, 18, 19. In particular, we characterize the photometric accuracy by a systematic offset between the empirical measure of noise and the pipeline-reported photometric uncertainty (Figs. 20, 21, 22).

6 Astrometry

Astrometry pertains to the measurement of the position of sources in the absolute World Coordinate System (WCS). Accurate and precise astrometry enables catalog cross-matching, and over long-term - measurement of proper motion of stellar sources.

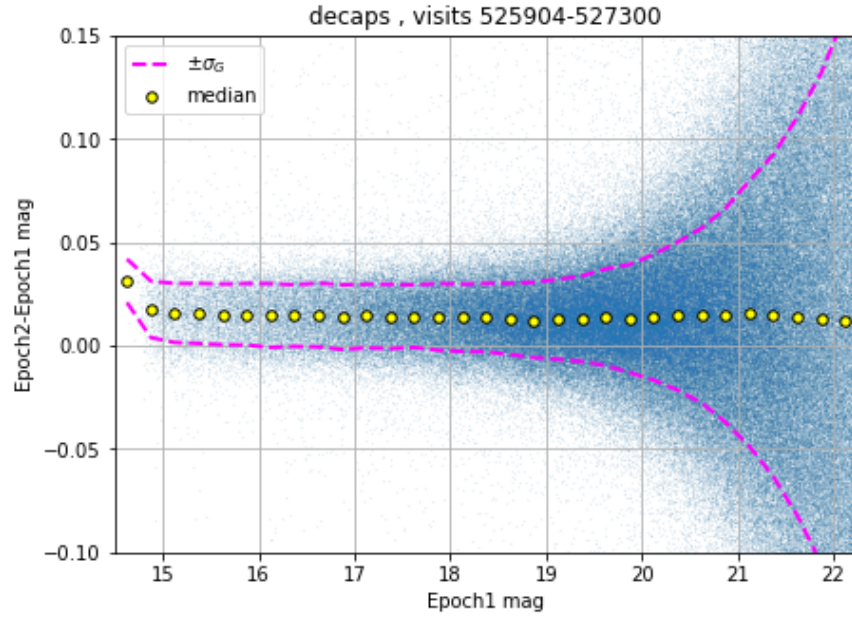


FIGURE 16: Similarly to Fig. 13, scatter plot of the magnitude difference between the two visits (525904, 527300) to the same sky region, separated by 2.95 days, processed by DECAPS. The magnitude difference is shown for all sources cross-matched between the two epochs, with a match within $0.5''$ - there is no selection on magnitude difference, but 0.5 mag (used for completeness) is well beyond the bounds of the plot, and would only remove the outliers to which neither median nor σ_G are sensitive. We overplot the $\pm\sigma_G$ envelope, and the median of each 0.25 mag bin.

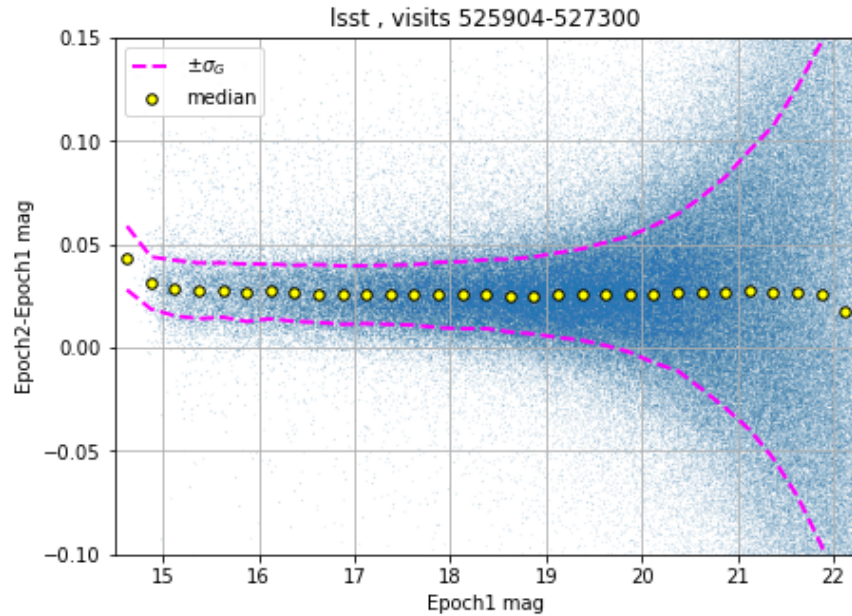


FIGURE 17: The same as Fig. 16, but for LSST processing of two visits to the same region, at two different epochs.

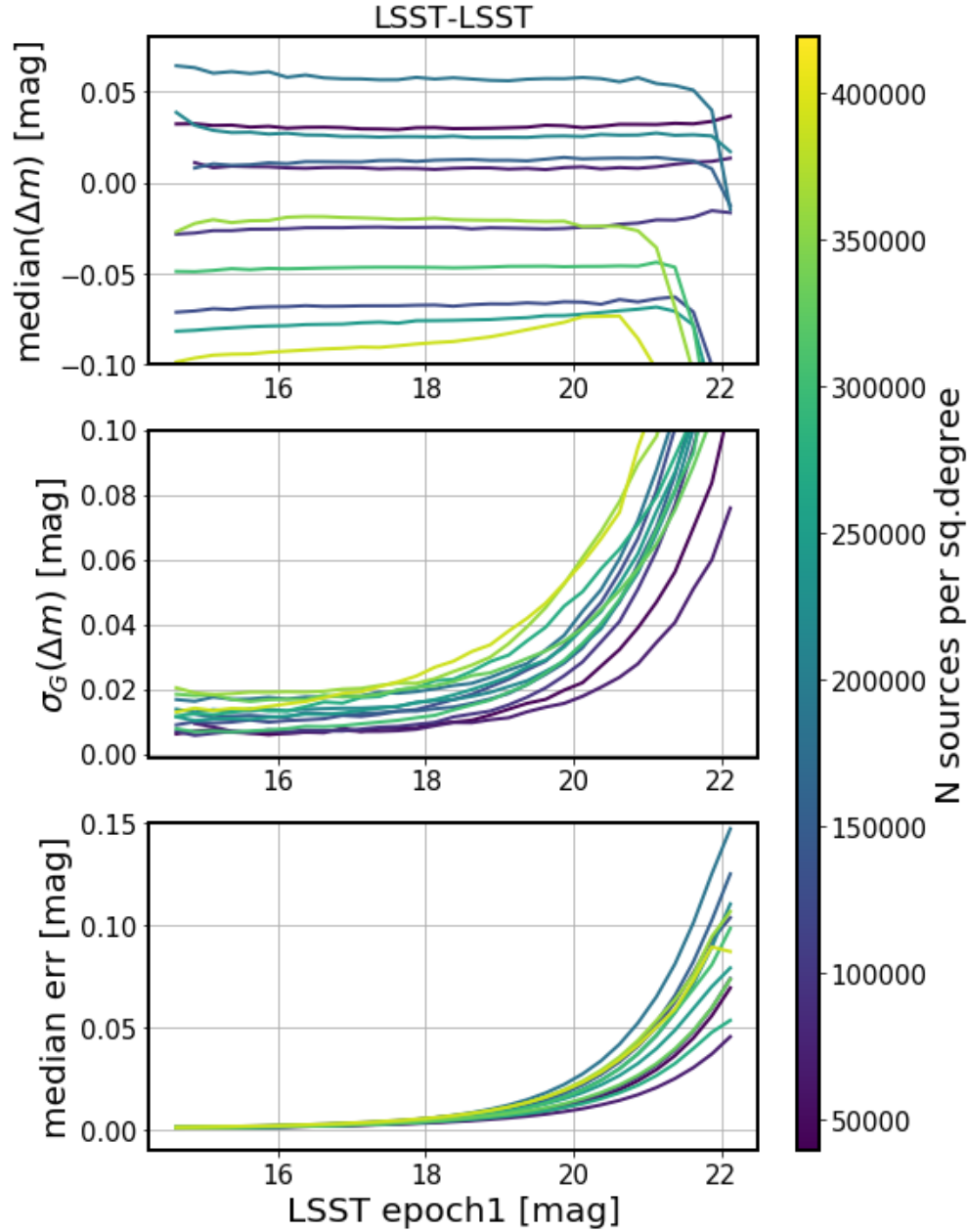


FIGURE 18: The internal repeatability test of the LSST pipeline. We cross-match the source catalogs for each visit. These two brightness measurements for the same source are akin to a two-epoch light curve. Since inherently variable sources constitute a small fraction of all stellar objects, and the majority of stars are not variable, the difference in the measured magnitudes would correspond to the empirical measure of noise. All sources cross-matched within $0.5''$ are binned according to their brightness. On the panels we plot, from top to bottom: median photometric offset, the robust interquartile-based measure of standard deviation σ_G , and the median reported measurement uncertainty.

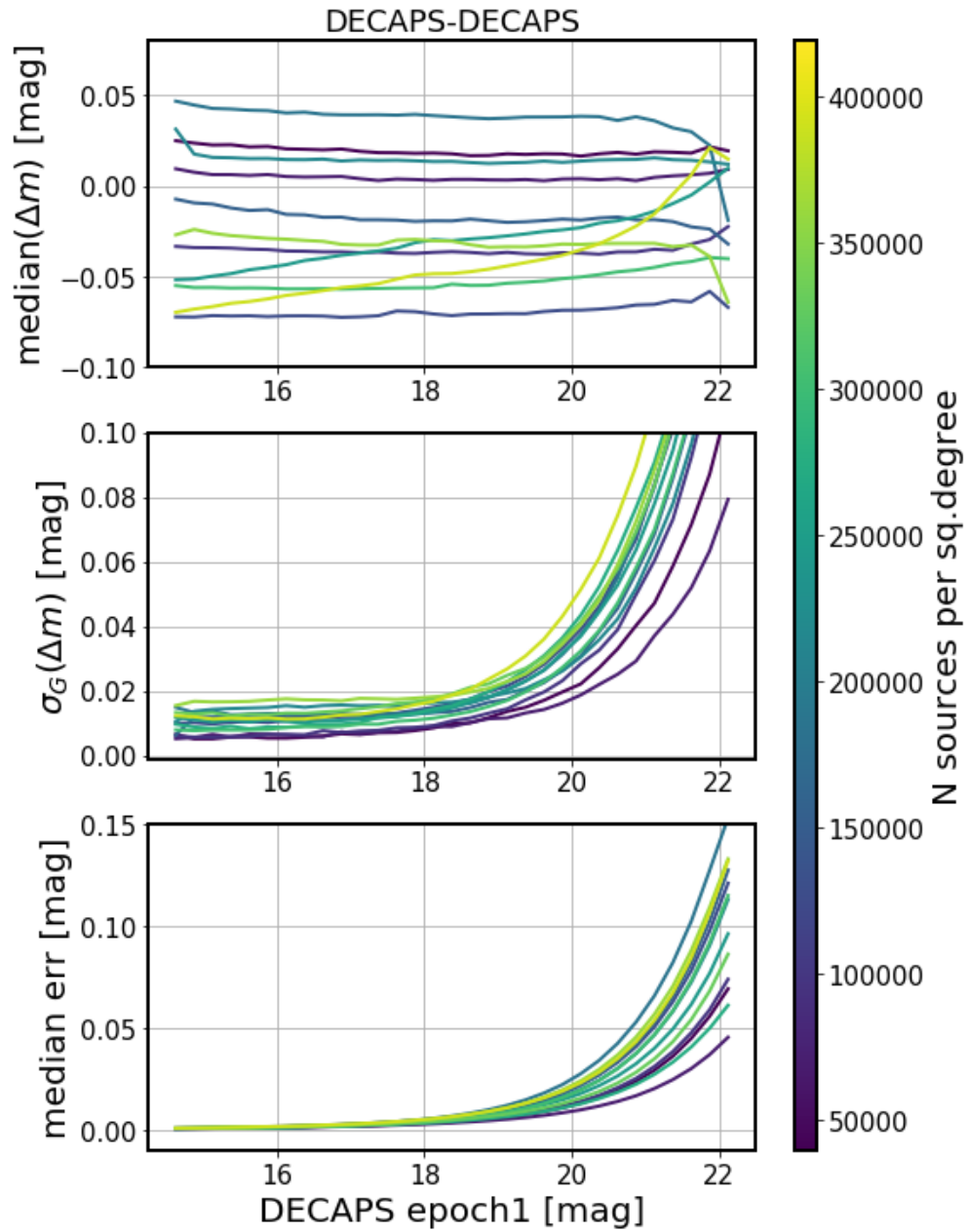


FIGURE 19: The internal repeatability test of DECAPS pipeline - for description, see Fig. 18.

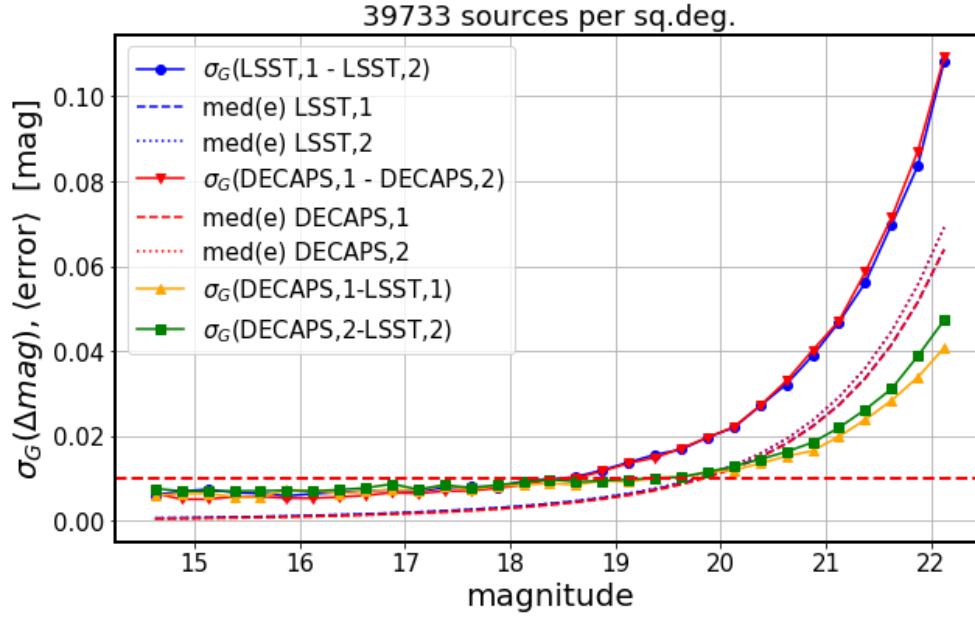


FIGURE 20: Comparison of spread of scatter between two pipelines vs. the empirical measurement of noise from repeatability for a pair of visits at the same location : 525846 and 530012, here called epoch1 and epoch2. All solid lines are $\sigma_G(a, b)$ - the interquartile-based measure of spread of magnitude difference between measurements a and b of the same source. From the top, $\sigma_G(LSST, 1 - LSST, 2)$, and $\sigma_G(DECAPS, 1 - DECAPS, 2)$, correspond to the empirical measure of noise. The blue line $\sigma_G(LSST, 1 - LSST, 2)$ is the same quantity as that plotted on the middle panel of Fig. 18, while the red line $\sigma_G(DECAPS, 1 - DECAPS, 2)$ is the same as that of Fig. 19. Then the dotted and dashed lines in the middle show the median error for epoch 1 or epoch 2, as reported by LSST or DECAPS pipelines. They represent the expected uncertainty in repeated measurement. Since they are identical, the red and blue dotted or dashed lines overlap. Finally, the green and orange solid curves correspond to the scatter between the two pipelines, calculated either for epoch1 ($\sigma_G(DECAPS, 1 - LSST, 1)$), or epoch2 ($\sigma_G(DECAPS, 2 - LSST, 2)$). Fig. 21 shows the second step in the analysis.

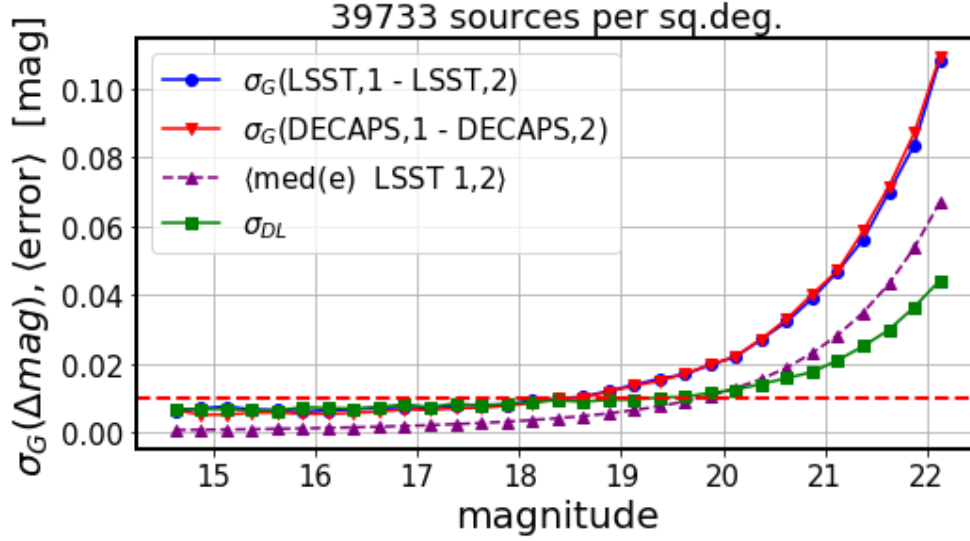


FIGURE 21: Second step in the analysis of photometric spread, following Fig. 20. The blue and red lines of repeatability are unchanged. Since LSST and DECAPS errors are almost identical, we choose to represent the minimum statistical offset by the mean LSST error between the two visits, added in quadrature. If e_{1L} and e_{2L} are LSST-reported error measurements for a given source for the two epochs, the quadrature-mean is $e_{12} = \sqrt{e_{1L}^2 + e_{2L}^2}/\sqrt{2}$, and the purple dashed line is the median of e_{12} per magnitude bin. We also add in quadrature the spread between the two pipelines, represented on Fig. 20 by orange $\sigma_{DL,1}$ for epoch1, and green $\sigma_{DL,2}$ for epoch2 : $\sigma_{DL} = \sqrt{\sigma_{DL,1}^2 + \sigma_{DL,2}^2}/\sqrt{2}$. Note that since the top blue (or red) lines $\sigma_G(LSST, 1 - LSST, 2)$, $\sigma_G(DECAPS, 1 - DECAPS, 2)$ (σ_{DD} , σ_{LL} for short) consists of noise σ_E and the systematic offset σ_S : $\sigma_{LL}^2 = \sigma_S^2 + \sigma_E^2$. Thus we calculate the systematic offset for LSST as $\sigma_S = \sqrt{\sigma_{LL}^2 - \sigma_E^2}$, which is the difference between blue solid and purple dashed lines.

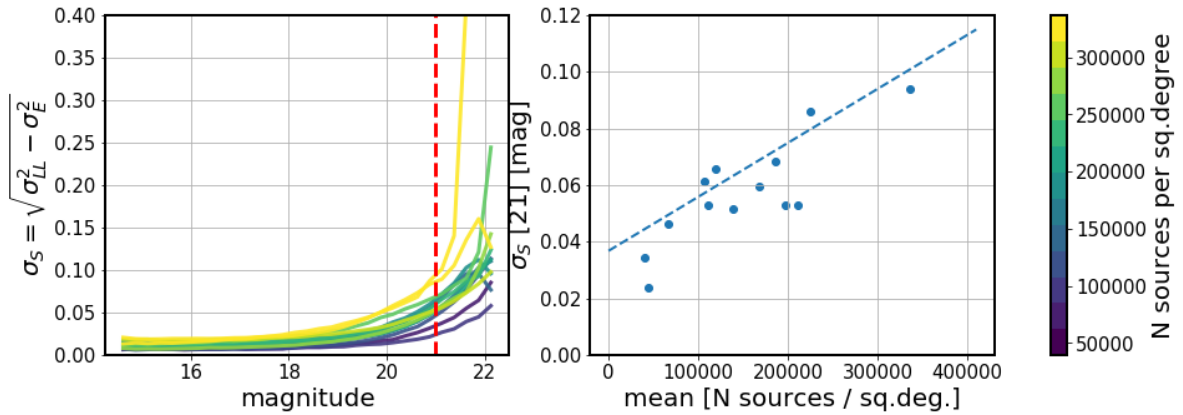


FIGURE 22: The left panel shows the measure of systematic offset between mean photometric error, and the photometric repeatability for the LSST pipeline as a function of magnitude (see Figs. 20, 21). Colors correspond to mean stellar density. Right panel shows σ_S at 21st magnitude as a function of stellar density.

TABLE 9: The difference in RA,DEC for various visits, between LSST processing of fields at the same location, but observed at different times (see Table 8 for summary). The median and spread of astrometric offset are in miliarcseconds. The final column shows the LSST source count averaged between the two visits in counts per square degree.

visit1	visit2	med($\Delta\alpha$)	med($\Delta\delta$)	$\sigma_G(\Delta\alpha)$	$\sigma_G(\Delta\delta)$	$\langle N \rangle$
525846	530012	1.83	0.18	9.43	8.85	39733
525900	529989	-3.12	0.36	10.87	11.58	44577
525814	529974	-0.29	1.15	10.65	10.46	66455
525838	527247	2.52	-2.23	9.96	12.21	94766
525837	527246	1.58	-1.24	9.07	11.51	110734
525920	527296	0.88	-3.2	10.36	9.85	119371
525904	527300	0.43	-1.55	8.29	10.0	138384
641497	644035	2.26	-1.42	19.8	22.68	167267
567283	645255	-5.58	1.05	33.77	19.75	185894
644082	527555	-4.16	-5.05	29.92	26.1	186731
527453	640995	-0.33	1.7	12.95	12.25	195763
525879	530032	0.8	-0.46	10.56	13.41	197058
527064	527552	-0.13	-2.19	16.93	15.74	224731
526028	641500	-1.2	0.42	11.52	11.12	281929
641548	644011	1.2	-2.43	26.08	30.7	336729
644144	566793	1.05	-0.25	27.86	19.69	339183
644074	644070	-2.56	0.3	26.14	27.69	419000

We consider two properties of successful astrometry. First, the internal consistency of a pipeline by measuring the repeatability of astrometric measurement between different epochs. Second - accuracy, and any biases between the LSST-DECAPS pipelines.

Part of the astrometric offset between the two pipelines is because DECAPS employed 2MASS-GAIA data (Fig.12 in [9]), whereas LSST used GAIA-TGAS data for astrometric calibration.

In all analysis the RA difference is corrected for the cosine of RA : $\Delta\alpha_{corr} = \delta\alpha \cos(\delta)$

To test the repeatability we use pairs of observations at the same location, as in Sec. 5.2. Fig. 23 shows an example of the LSST-LSST comparison, with Fig. 24 showing the magnitude dependence. Fig. 25 depicts the offset in RA , DEC , for DECAPS-DECAPS comparison.

To test possible offset between LSST and DECAPS astrometric solutions, on Fig. 28 we find the offset in measured RA , DEC for sources cross-matched in catalogs from the two pipelines.

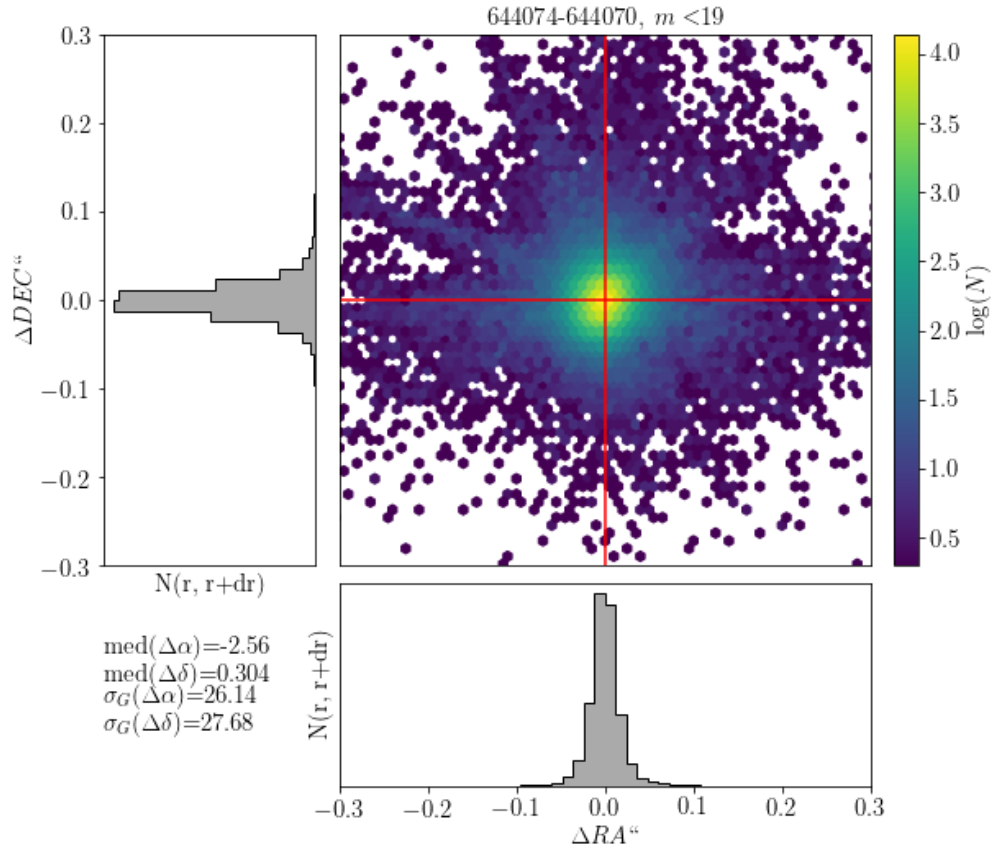


FIGURE 23: The difference of LSST processing for RA,DEC for visits 644074,644070: a pair of visits at the same location, separated by less than a day. The mean number of sources is 419000 sources per sq.deg., which corresponds to top 1% of the sky. We select sources brighter than 19 magnitude. For all other pairs the offsets are all centered on zero with similar spread - see Table 9

LSST processing, visits 644074-644070 mean 419000 sources per sq.deg.

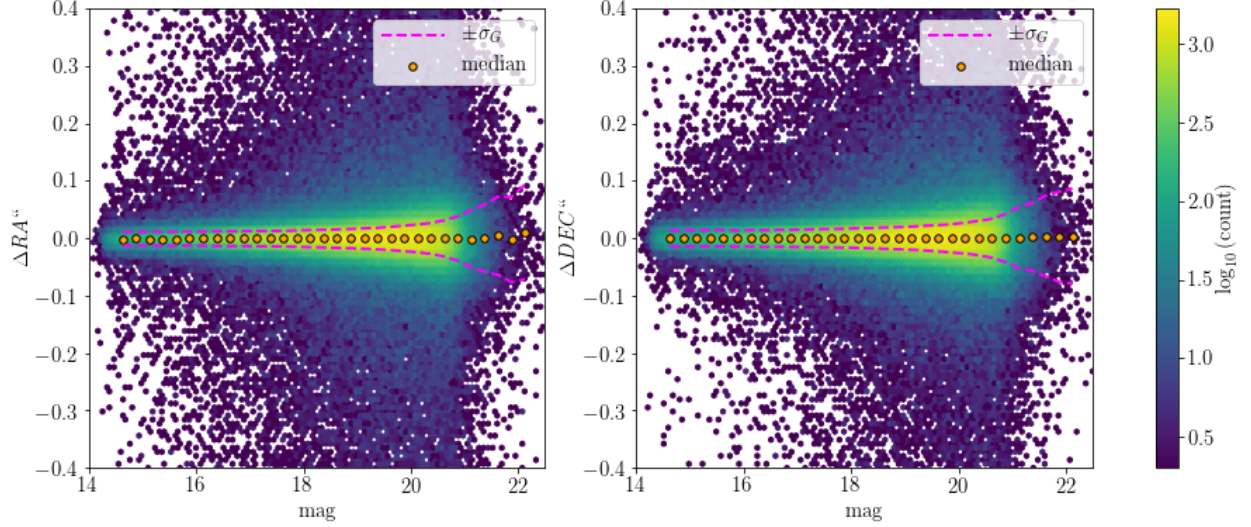


FIGURE 24: The difference in RA,DEC for the same visits as on Fig. 23, shown as a function of magnitude.

TABLE 10: The difference in RA,DEC for various visits, between DECAPS processing of fields at the same location, but observed at different times (see Table 8 for summary). All measured quantities are in miliarcseconds. See Table 9 for the equivalent visits processed by LSST.

visit1	visit2	med($\Delta\alpha$)	med($\Delta\delta$)	$\sigma_G(\Delta\alpha)$	$\sigma_G(\Delta\delta)$	$\langle N \rangle$
525846	530012	5.92	-1.18	14.69	14.49	39733
525900	529989	-5.34	-4.18	21.18	20.76	44577
525814	529974	6.55	0.19	20.58	17.76	66455
525838	527247	-6.5	-0.72	17.62	16.45	94766
525837	527246	-3.55	-2.86	18.5	17.57	110734
525920	527296	-4.97	-3.26	19.72	16.88	119371
525904	527300	-5.05	-4.13	14.4	16.26	138384
641497	644035	8.91	12.57	34.18	31.02	167267
567283	645255	-53.12	-49.23	39.71	24.55	185894
644082	527555	139.33	-15.63	40.71	36.27	186731
527453	640995	-126.51	28.81	24.75	18.27	195763
525879	530032	-0.43	-5.17	22.88	23.66	197058
527064	527552	5.11	-3.74	20.95	25.13	224731
526028	641500	-134.26	28.5	26.81	19.56	281929
641548	644011	-1.69	-5.63	32.3	36.95	336729
644144	566793	94.95	68.82	32.42	23.74	339183
644074	644070	-4.92	1.61	25.15	28.14	419000

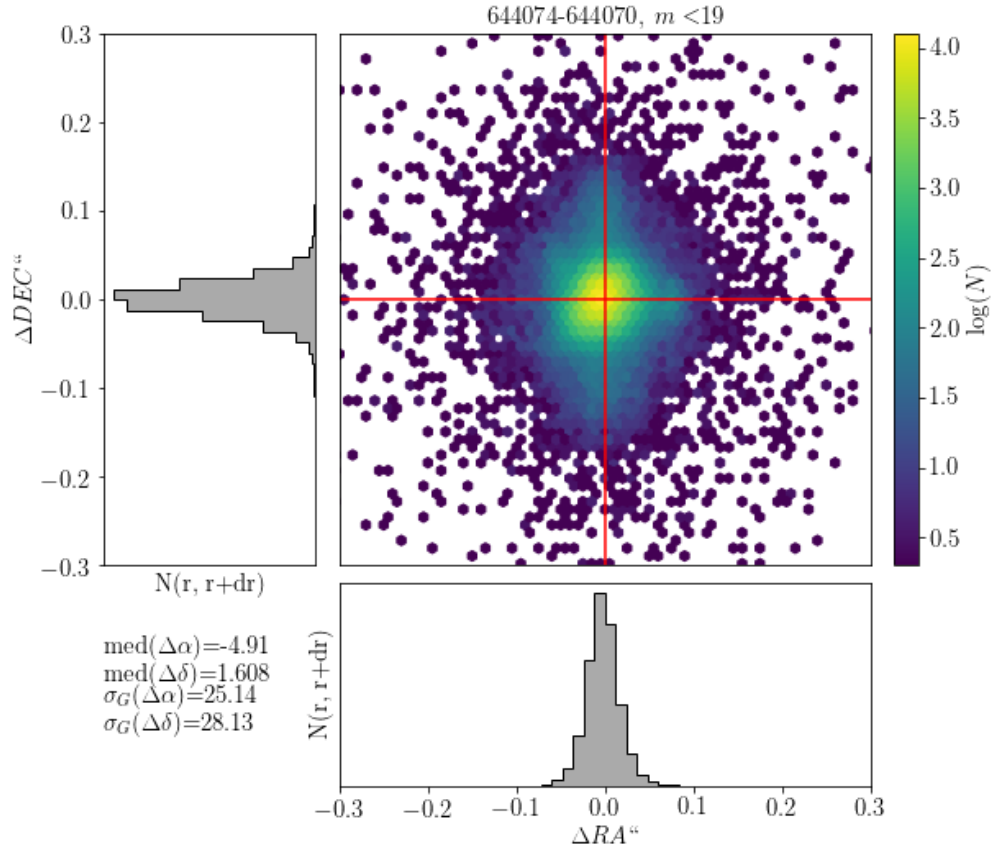


FIGURE 25: The difference in RA,DEC for the same visits as in Fig. 23, but comparing DECAPS single-epoch catalogs. The spread of $\Delta\alpha$, $\Delta\delta$ is wider than for equivalent visit pairs processed by the LSST Science Pipelines - see Table 10

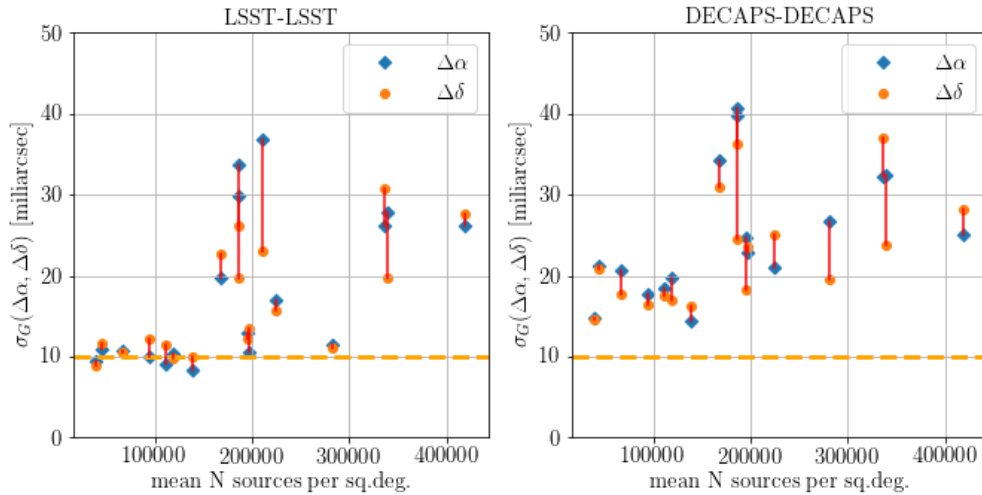


FIGURE 26: Summary of LSST and DECAPS repeatability of astrometry, as in Tables 9 and 10.

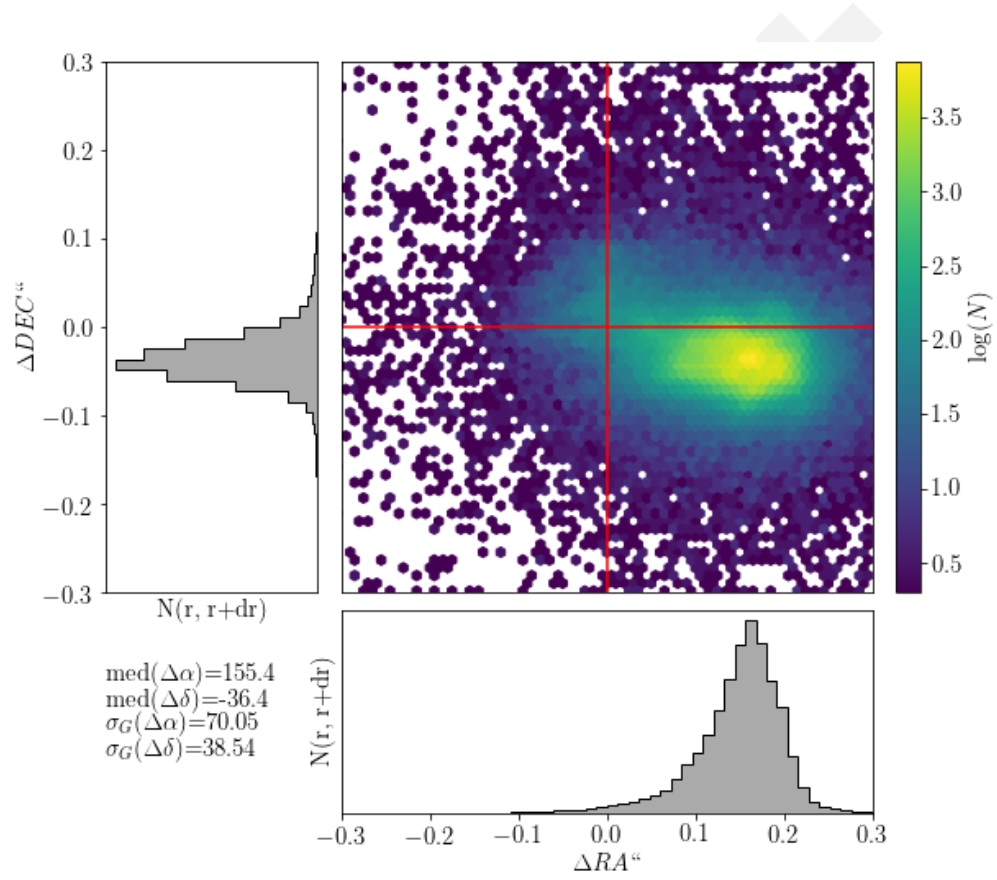


FIGURE 27: The difference in RA,DEC for visit 525904 , between LSST and DECAPS processing (402270 detected sources in the clean LSST catalog). We tested that for other vists and in all cases the offset position and magnitude remains the same - see Table 11

TABLE 11: The difference in RA,DEC for the same visit analyzed by LSST and DECAPS. Each row corresponds to a separate visit, which correspond to different stellar density. All measured quantities are in miliarcseconds.

visit	median($\Delta\alpha$)	median($\Delta\delta$)	$\sigma_G(\Delta\alpha)$	$\sigma_G(\Delta\delta)$
525904	155.49	-36.46	70.06	38.55
525920	130.45	-27.53	72.83	43.88
525846	105.62	-51.71	42.49	30.04
525879	131.93	-42.62	138.58	75.68
525837	96.01	-47.93	65.17	36.6
525838	124.9	-68.92	59.56	33.99
525814	39.99	-29.87	47.26	29.72
525900	127.61	-32.38	54.81	33.67
527300	146.26	-38.73	56.49	25.48
527296	120.47	-26.98	41.65	27.14
530012	111.21	-51.38	35.01	28.34
530032	126.69	-47.85	115.02	65.23
527246	88.38	-49.06	45.87	30.6
527247	110.44	-66.18	43.15	29.71
529974	49.13	-30.91	48.55	28.95
529989	126.51	-33.77	52.12	28.33

7 Conclusions

7.1 LSST Processing of StarFast Simulated Sky

An independent way to further test the performance of the LSST Science Pipelines is to use the simulated sky images, where the true position and brightness of each source is known. This would put the measure of source detection completeness, photometric and astrometric precision on an absolute scale. We already tested a StarFast image simulator¹², and confirmed that it can successfully simulate a region of the sky seeded with known stellar population.

7.2 Other LSST-DECAPS tests: w-color

An independent test of the quality of photometry would be to consider the width of the stellar locus ('w-color') on the g-r vs r-i color-color plot. This could be used to test internal consistency of LSST and DECAPS photometry.

¹²<https://dmtm-012.lsst.io>

References

- [1] Bosch, J., et al. 2017, ArXiv e-prints 1705.06766
- [2] Hogg, D. W. 2001, The Astronomical Journal, 121, 1207
- [3] Lupton, R. 2005, in prep.
- [4] Lupton, R., Gunn, J. E., Ivezić, Z., Knapp, G. R., & Kent, S. 2001, in Astronomical Society of the Pacific Conference Series, Vol. 238, Astronomical Data Analysis Software and Systems X, ed. F. R. Harnden, Jr., F. A. Primini, & H. E. Payne, 269
- [5] Lupton, R. H., Ivezić, Z., & Gunn, J. 2005, in prep.
- [6] Lupton, R. H., Ivezić, Z., Gunn, J. E., Knapp, G., Strauss, M. A., & Yasuda, N. 2002, in SPIE Proceedings, Vol. 4836, Survey and Other Telescope Technologies and Discoveries, ed. J. A. Tyson & S. Wolff, 350
- [7] Narayan, G., et al. 2018, ArXiv e-prints
- [8] Olsen, K. A. G., Blum, R. D., & Rigaut, F. 2003, AJ, 126, 452
- [9] Schlafly, E. F., et al. 2017, ArXiv e-prints 1710.01309
- [10] Shaw, R. A. 2015, NOAO Data Handbook